This is a preprint, the final version is subject to change, of the American Mineralogist (MSA)
Cite as Authors (Year) Title. American Mineralogist, in press.
DOI: https://doi.org/10.2138/am-2018-6224

Revision 4

Titanite major and trace element compositions as petrogenetic-metallogenic indicators: Examples from four granite plutons in the southern Yidun arc, SW China

Li-Chuan Pan[a], Rui-Zhong Hu[a,b]*, Xian-Wu Bi[a], Chusi Li[c], Xin-Song Wang[a], Jing-Jing Zhu[a]

[a]State Key Laboratory of Ore Deposit Geochemistry, Institute of Geochemistry, Chinese Academy of Sciences, Guiyang 550000, China

[b]University of Chinese Academy of Sciences, Beijing 100039, China

[c]Department of Earth and Atmospheric Sciences, Indiana University, Bloomington, IN 47405, USA

* Corresponding author email, huruizhong@vip.gyig.ac.cn Fax, +86-851-5891664
e-mail, huruizhong@vip.gyig.ac.cn

Abstract

Major, minor, and trace element abundances in titanite crystals from four granitic plutons in southern Yidun arc, SW China have been determined using electron microprobe and laser ablation inductively coupled plasma mass spectrometry. The selected plutons are the Cretaceous Xiuwacu (CXWC) pluton, with quartz vein-type Mo mineralization (economic-Mo), the Tongchanggou (TCG) pluton, with porphyry-type Mo mineralization (economic-Mo), the Triassic Pulang (PL) pluton, with porphyry-type Cu mineralization (subeconomic-Mo), and the Triassic Xiuwacu (TXWC) pluton, without any Mo mineralization (Mo-barren). Our study reveals that the chemical compositions of titanite crystals from these plutons, such as REE, Sr, Ga, δEu, δCe, Fe_2O_3/Al_2O_3, halogen and Mo can be used to track magma compositions, oxidation states, metal fertility and crystallization history. The data from this study also show that titanite crystals from these plutons with different potential of Mo mineralization have similar Mo contents and exhibit an irregular variation between Mo and Sr abundances (indicating non-Mo enrichment in residual melt during the progressive crystallization) for some Mo-mineralized plutons. Our new observations support the recent hypothesis that high initial Mo contents in magma and the enrichment of Mo in residual melts formed by fractional crystallization are not the only requirements to form a granite-related Mo ore deposit. Efficient extraction of the residual melts, possibly facilitated by high concentrations of magmatic F is also critical to the ore formation. Evidence for high F concentration in felsic magma, which facilitates melt and fluid separation and economic Mo mineralization during magma evolution, may be traced by the presence of F-rich titanite crystals in the two Mo-mineralized granite plutons (CXWC and TCG). These new findings from this study confirm that titanite is indeed a good petrogenetic-metallogenic indicator. However, in light of the limited contribution of metal fertility to Mo mineralization, we suggest that titanite Mo concentrations should be used along with other crucial proxies, such as titanite F contents and Fe_2O_3/Al_2O_3 ratios to better evaluate the Mo-mineralized potential of granites.

Key words: Titanite; LA-ICP-MS; REE; Oxidation state; Magma composition; Mo mineralization; Ore genesis

Introduction

The chemical compositions of minerals in igneous rocks are widely used to track magma evolution. With respect to trace element compositions, accessory minerals are more useful than major rock-forming minerals because the accessory minerals contain much large amounts of important trace elements such as REEs and HFSEs and are less susceptible to alteration and weathering. Titanite ($CaTiSiO_5$) is an important accessory mineral in granites (Nakada 1991; Bachmann et al. 2005; Glazner et al. 2008). It is robust, and therefore preserves its original geochemical signature even after post-emplacement alteration (Selvig et al. 2005). Titanite is a major carrier of REE and HFSE in granites and thus can be used to track felsic magma evolution (Hayden et al. 2008; Tiepolo et al. 2002; Buick et al. 2007). For example, titanite crystallization may significantly affect whole-rock Nb/Ta, Zr/Hf and REE ratios (Wolff 1984; Wolff and Storey 1984; Prowatke and Klemme 2005; Marks et al. 2008; Glazner et al. 2008).

It is well known that titanite is a good petrogenetic-metallogenic indicator. For example, Zr in titanite has been used to estimate its saturation temperature in magma (Hayden et al. 2008). Substitution of Ti^{4+}+O^{2-} by Al^{3+}+F^{-} in the titanite structure is known to be a function of temperature and pressure (Tropper and Manning 2008). The Ga content and δCe of titanite have been used to evaluate the oxidation state of magma (King et al. 2013; Xu et al. 2015). The cotectic ratio of titanite and ilmenite is also a function of the oxidation state of magma and has been used to estimate redox conditions (Carmichael and Nicholls, 1967; Wones 1989; Frost et al. 2000). The concentrations of Sn, W and Mo in titanite are good indicators of magma fertility for these metals (Aleksandrov and Troneva 2007; Xie et al. 2010; Wang et al. 2013; Che et al. 2013). In addition, titanite is also a good U-Th-Pb radiometric chronometer (Corfu and Muir 1989; Pidgeon et al. 1996; Essex and Gromet 2000; Frost et al. 2000; Buick et al. 2007; Li et al. 2010).

It is well known that titanite is a good petrogenetic-metallogenic indicator, and has been successfully used in the studies of granitoids worldwide (e.g., Piccoli et al. 2000; Wang et al. 2013; Bruand et al. 2014; Xu et al. 2015; Jiang et al. 2016). In this study, we use the major and trace element compositions of titanite from four granite plutons in the Mesozoic Yidun arc in SW China to study the magma evolution, the factors controlling Mo mineralization, and the Mo mineralization potential of these granites. The selected plutons are of Triassic to Cretaceous ages and are all I-type granites (typical or highly fractionated) (Wang et al. 2011; Wang et al. 2014a; Liu et al. 2017). Among the selected plutons, the Xiuwacu (Cretaceous), Tongchanggou and Pulang host hydrothermal vein type Mo mineralization, porphyry type Mo mineralization (both economic-Mo) and porphyry type Cu mineralization with weak Mo mineralization (subeconomic-Mo) respectively, while the Xiuwacu (Triassic) pluton does not contain any type of hydrothermal Mo mineralization (Mo-barren).

These data show that the chemical compositions of titanite crystals, such as the REE (especially δEu, δCe), Sr, Ga, halogen and Mo compositions, and Fe_2O_3/Al_2O_3 ratios are good proxies to track magma composition, oxidation state, metal fertility and crystallization history. Based on these magmatic properties revealed by titanite chemistry, we further discussed the controlling mechanisms of granite-related Mo mineralization operating in these districts. Our new results provide a further evidence supporting an important conclusion made recently by Lerchbaumer and Audėtat (2013), that high initial magmatic Mo contents and extreme enrichment of Mo by fractional crystallization is not sufficient to form economic Mo mineralization. Efficient Mo extraction during magma evolution, possibly facilitated by high concentrations of magmatic F, is also required for the formation of a granite-related Mo ore deposit.

Geology and Petrology

The four selected granite plutons occur in the southern part of the Mesozoic Yidun arc that is bound by the Qiangtang block to the west and the Yangtze Craton to the east (Fig. 1). Regional magmatism mainly occurred from Triassic to Cretaceous during the westward subduction of the Garzê-Litang oceanic plate and the post-collisional lithospheric rifting or delamination (Li et al. 2007; Peng et al. 2015), with two major peaks at 230-215 and 110-80 Ma (Wang et al. 2011; Wang et al. 2014a). The igneous rocks are dominated by I-type granites that mainly formed by the partial melting of the crust with Rittmann index <3.3, A/CNK ~1.0, $(^{87}Sr/^{86}Sr)_i$ >0.7056, and negative $\varepsilon_{Nd}(t)$ (Wang et al. 2011; Leng et al. 2014; Wang et al. 2014a; 2014b; Zu et al. 2016). Hydrothermal Cu and Mo mineralization is present in some of the plutons. The characteristics and genesis of Mo and Cu mineralization associated with some of the granite plutons in the region have been well documented and discussed in many previous studies (e.g., Li 2007; Li et al. 2014; Wang et al. 2014a; 2014b; 2015; Yu and Li 2014; Yu et al. 2015).

We selected four representative plutons, including Mo-Cu mineralized and unmineralized varieties. The extent of Mo mineralization decreases from economic in the Tongchanggou (porphyry type) and Cretaceous Xiuwacu plutons (Qz-vein type) to sub-economic in the Pulang pluton (porphyry type, Cu-dominant). The Triassic Xiuwacu pluton represents a Mo completely unmineralized endmember. The parental magmas of the TCG and CXWC plutons were derived from the Cretaceous within-plated setting, while that of the PL and TXWC plutons were derived from the Triassic island arc setting. While these plutons represent a variety of ages and tectonic settings, we chose them because they exemplify different endowments of Mo mineralization and provide an opportunity to use titanite chemistry to test what geologic mechanisms control Mo mineralization in these districts.

The Cretaceous Xiuwacu (CXWC) pluton

The CXWC pluton is located ~50 km northwest of the Shangri-La city (Fig. 1). This pluton consists of three zones: biotite granite, monzogranite and leucogranite (Fig. 2a). The major rock-forming minerals are biotite, hornblende, plagioclase, K-feldspar and quartz. The accessory minerals are apatite, allanite, zircon and titanite. Titanite has been found only in the biotite granite and monzogranite zones. Hydrothermal vein type Mo mineralization (~0.20 Mt Mo) is mainly associated with biotite granite and monzogranite zones. The zircon U–Pb age of this pluton is ~85 Ma (Wang et al. 2014a; 2014b). The whole rocks have $(^{87}Sr/^{86}Sr)_i$ from 0.7075 to 0.7085, $\varepsilon_{Nd}(t)$ from −6.9 to −7.6, and zircon $\delta^{18}O$ from 5.9‰ to 8.4‰. These isotope characteristics suggest that the parental magma was formed by the partial melting of lower continental crust (Wang et al. 2014b).

The Tongchanggou (TCG) pluton

The TCG pluton is located ~15 km southeast of the Shangri-La city (Fig. 1). It is mainly composed of biotite granitic porphyry (Fig. 2b), with abundant plagioclase, biotite and quartz phenocrysts. The matrix is composed of fine-grained plagioclase, K-feldspar, quartz, biotite and hornblende. Apatite, titanite and zircon occur as accessory phases in the matrix. This pluton hosts a large porphyry Mo deposit with proven reserves of nearly 0.30 Mt Mo. The zircon U–Pb age of this pluton is ~87 Ma (Wang et al. 2014a). The whole rocks have $(^{87}Sr/^{86}Sr)_i$ of 0.7069 and $\varepsilon_{Nd}(t)$ from −5.3 to −5.6. Combined with the slight Eu anomalies (δEu from 0.9 to 1), high ratios of $(La/Yb)_N$ (>30), and low concentrations of Y(<18ppm) and Yb (<1.9ppm), these data suggest this adakitic parental magma was derived from the partial melting of thickened lower continental crust (Wang et al. 2014b).

The Pulang (PL) pluton

The PL pluton is located ~36 km northeast of the Shangri-La city (Fig. 1). It consists of quartz diorite porphyrite, quartz monzonitic porphyry and granodiorite units (Fig. 2c). The quartz monzonitic porphyry unit hosts a porphyry Cu deposit with weak Mo mineralization (~0.01 Mt Mo). The host rock is composed of K-feldspar, plagioclase, biotite and quartz as phenocrysts and fine-grained plagioclase, K-feldspar, quartz, biotite as matrix. Apatite, titanite and zircon are accessory phases in the matrix. The zircon U–Pb age of the pluton varies from 211 to 230 Ma (Wang et al. 2011; Pang et al. 2014). The whole rocks have $(^{87}Sr/^{86}Sr)_i$ of 0.7065 and $\varepsilon_{Nd}(t)$ of −3.0, which supports the notion that the parental magma was probably derived from the partial melting of the subducted oceanic slab (Li et al. 2007; Pang et al. 2014).

The Triassic Xiuwacu (TXWC) pluton

The TXWC pluton is located ~85 km northwest of Shangri-La city (Fig. 1). It is dominated by biotite granite (Fig. 2a) that is composed of biotite, K-feldspar, plagioclase, biotite and quartz. The accessory minerals are apatite, titanite and zircon. No significant Mo mineralization is associated with this pluton. The zircon U–Pb age and $\varepsilon_{Hf}(t)$ of this pluton are ~202 Ma and from -2.9 to 4.1, respectively, which is consistent with the hypothesis that this pluton also formed from magma produced by partial melting of the subducted oceanic slab (Liu et al. 2017).

Analytical methods

The whole rock samples used in this study are relatively fresh and do not contain significant Mo-Cu mineralization. The concentrations of major elements in whole rocks were determined with fused lithium tetraborate glass pellets using an Axios PW4400 X-ray fluorescence spectrometer at the State Key Laboratory of Ore Deposit Geochemistry, Institute of Geochemistry, Chinese Academy of Sciences in Guiyang. The analytical precision is estimated to be within 5%. The concentrations of trace elements in whole rocks were analyzed using a PE DRC-e ICP-MS at the same laboratory described above. Powdered samples (50 mg) were dissolved using HF and HNO_3 acids mixture in high-pressure Teflon bombs for 2-days at about 190^{o}C. Rh was used to monitor signal drifting during analysis. The detailed analytical procedures are given in Qi et al. (2000). The analytical precision is estimated to be within 10%.

Titanite crystals were separated from the samples using standard heavy-liquid and magnetic methods, followed by hand-picking under microscope. The titanite grains were mounted in epoxy, polished, and examined using CL and BSE images to select suitable targets for *in situ* analysis. The selected analytical targets are at the center of titanite crystals, in order to minimize the effect of subsolidus exchange reaction between titanite and the surrounding minerals.

The contents of major and minor elements in titanite were determined using a JOEL-1600 electron microprobe at the above-mentioned laboratory. The analytical conditions are 25 kV accelerating voltage, 10 nA beam current, and 10 μm beam diameter. The following natural minerals were used for calibration: rutile (Ti), pyrope garnet (Si, Al, Mg, Fe, Mn), albite (Na), apatite (Ca, P), and phlogopite (F). The detection limits are 0.04 wt.% for F,0.03 wt.% for Ti, 0.02 wt.% for Mn and Fe, and 0.01wt.% for Ca, Si, Na, Al, Mg and P.

The concentrations of trace elements in titanite were measured by *in situ*

LA-ICP-MS at the above-mentioned laboratory, following the analytical procedures and operation conditions given in Tu et al. (2011). The LA-ICP-MS system consists of an Agilent 7500a ICP-MS equipped with a Resonetics RESOLution M-50 ArF-Excimer laser gun (λ = 193 nm, 80 mJ, 10 Hz). The laser ablation spot is 30 μm in diameter. The ablated aerosol was fed to the ICP instrument using He gas. The content of Ca was measured using ^{43}Ca and normalized using the concentration determined by electron probe analysis. The NIST610 standard was used for calibration and the NIST612 standard was used as standard reference. Off-line data reduction was done using the ICPMSDataCal software from Liu et al. (2008). The detection limits by LA-ICP-MS are estimated to be <0.3 ppm for Sm and Gd, and <0.1 ppm for U, Th, Sr, Zr, Ga and other REE.

In order to determine the magmatic oxidation states, trace elements in zircon from these four plutons were determined by LA-ICP-MS at the above-mentioned laboratory. Zircon was sampled by a GeoLasPro laser-ablation system. Ion-signal intensities were acquired through an Agilent 7700x ICP-MS instrument with Helium (He) as the carrier gas. Ablation protocol employed a spot diameter of 44 μm at 4 Hz repetition rate. The NIST610 standard was used for calibration and the NIST612 standard was used as standard reference. Off-line data reduction was done using the ICPMSDataCal software from Liu et al. (2008). The detection limits for trace elements in zircon by LA-ICP-MS are estimated to be <0.4 ppm for Hf, <0.2 ppm for Nd, and <0.1 ppm for U, Th, Y, Nb, Ta and other REE.

Results

Whole-rock compositions

Major and minor elemental compositions of the rock samples from the four selected granite plutons are listed in Table 1. They are metaluminous, calc-alkaline granitoids (Fig. 3a; b) with a Rittmann index of 2.00–2.75 and A/CNK of 0.94–1.00. The samples from the CXWC pluton have higher SiO_2 (71.19–76.19 wt.%) but lower CaO (0.63–1.45 wt.%) and MgO (0.10–0.55 wt.%) than the other plutons. The samples from the TCG pluton have SiO_2 from 64.6 to 65.8 wt.%, CaO from 2.9 to 3.8 wt.%, and MgO from 1.2 to 1.4 wt.%; the samples from the PL pluton have SiO_2 from 61.7 to 65.0 wt.%, CaO from 2.7 to 3.5 wt.%, and MgO from 2.4 to 4.0 wt.%;the samples from the TXWC pluton have SiO_2 from 68.3 to 70.3 wt.%, CaO from 2.4 to 3.0 wt.%, and MgO from 1.0 to 1.7 wt.%.

The chondrite-normalized trace element patterns of the samples are illustrated in Fig. 4a. All of the samples from the different plutons are characterized by mild to strong depletions in K, Sr, P, and Ti. Except the samples from the CXWC pluton, all of the samples from the other plutons are also characterized by negative Nb-Ta anomalies. In the chondrite-normalized REE diagram, all of the samples from the four selected plutons display fractionated REE patterns (Fig. 4b). The samples from the TCG pluton have the highest values of $(La/Yb)_N$ from 35 to 46, $(La/Sm)_N$ from 7.4 to 8.6, $(Sm/Yb)_N$ from 7.4 to 5.3, and δEu from 0.9-1. The samples from the PL and TXWC plutons have medium REE ratios: the PL pluton has $(La/Yb)_N$ from 13.2 to 14.5, $(La/Sm)_N$ from 3-3.5, $(Sm/Yb)_N$ from 4.2 to 4.5, and δEu from 0.73-0.75 while the TXWC pluton has $(La/Yb)_N$ from14.7 to 20, $(La/Sm)_N$ from 4.8 to 6.1, $(Sm/Yb)_N$ from 2.8 to 3.3, and δEu from 0.75 to 0.8. The lowest REE ratios are shown by the samples from the CXWC pluton: $(La/Yb)_N$ from 2.3 to 21, $(La/Sm)_N$ from 2.2 to 6.7, $(Sm/Yb)_N$ from 0.98 to 3.2, and δEu from 0.1 to 0.6.

Major and minor elements in titanite

The titanite crystals from the four selected granite plutons have similar major element compositions: 26-28 wt.% CaO, 34-36 wt.% TiO_2 and 29-31 wt.% SiO_2. The average contents of F in titanite crystals from the CXWC pluton are up to 1 wt.%, much higher than those from the other plutons (<0.5 wt.%). The average contents of (Fe_2O_3+Al_2O_3) in titanite crystals from the CXWC pluton are up to 4.2 wt.%, significantly higher than the value (<3.4 wt.%) in titanite crystals from the other plutons. The average contents of MnO in titanite crystals from the CXWC, TCG and TXWC plutons can be up to 0.14 wt.%. The contents of MnO in most of the titanite crystals from the PL plutons are below the detect limit by EMPA (0.02 wt.%). The contents of Na_2O, P_2O_5 and MgO in titanite crystals from all four selected granite plutons are close to or below the detection limits.

The co-variations in concentrations of Ca, F, TiO_2, and Fe_2O_3+Al_2O_3 in titanite crystals can be seen Fig. 5. The factors controlling these co-variations will be discussed below.

Trace elements in titanite

REE-Y

Among the four selected granite plutons, the total REE content in titanite are the highest in the TXWC pluton (1.97 wt.%), medium in the PL pluton (1.63 wt.%) and the TCG pluton (1.49 wt.%), and the lowest in the CXWC pluton (1.15 wt.%). Although Y and REE are believed to have similar partitioning behavior in magmatic process, the magnitude of Y contents is different from the magnitude of REE contents in titanite. Among the four selected plutons, titanite crystals in the TXWC and CXWC plutons have higher Y contents (3700-5700 ppm). Titanite crystals in the other two plutons have lower Y contents (1900-2700 ppm).

The magnitude of REE ratios of titanite and whole rock samples from the four selected granite plutons are similar. Similar to whole rock REE trends, titanite crystals from the TCG pluton have the highest values of $(La/Yb)_N$ from 4.2 to 16.1, $(La/Sm)_N$ from 0.76 to 2.2, $(Sm/Yb)_N$ from 4.2 to 9.4, and δEu from 0.6 to 0.9. Titanite crystals from the PL and TXWC plutons have medium REE ratios: the PL titanite crystals have $(La/Yb)_N$ from 2.8 to 11, $(La/Sm)_N$ from 0.6 to 2.9, $(Sm/Yb)_N$ from 3.8 to 6.4, and δEu from 0.56-0.69 while the TXWC titanite crystals have $(La/Yb)_N$ from 1.1 to 3.3, $(La/Sm)_N$ from 0.5 to 0.9, $(Sm/Yb)_N$ from 1.7 to 5.9, and δEu from 0.27 to 0.57. Titanite crystals from the CXWC pluton have the lowest REE ratios: $(La/Yb)_N$ from 0.9 to 7.8, $(La/Sm)_N$ from 0.4 to 1.5, $(Sm/Yb)_N$ from 1.7 to 5.3, and δEu from 0.17 to 0.51. The values of δCe are very close in these four plutons (~1.0), but are more variable in titanite crystals from these plutons (1.12-1.27).

Nb-Ta-Th-U

Titanite is a very important sink of the whole-rock Nb, Ta, Th, and U. The Nb and Ta contents in titanite crystals from the four selected granite plutons are positively correlated. Titanite crystals from the CXWC pluton have the highest average concentrations of Nb (6227 ppm) and Ta (983 ppm). Titanite crystals from the TXWC and TCG plutons have medium average Nb and Ta contents: the TXWC titante crystals have 4460 ppm Nb and 599 ppm Ta while the TCG titanite crystals have 3007 ppm Nb and 282 ppm Ta. Titanite crystals from the PL pluton have the lowest average contents of Nb (1410 ppm) and Ta (184 ppm).

The concentrations of Th and U in titanite crystals from the four selected granite plutons are negatively correlated. Titanite crystals from the PL pluton contain the highest Th (527 ppm) and the lowest U (70 ppm). Titanite crystals from the CXWC pluton contain the lowest Th (183 ppm) and the highest U (190 ppm). Titanite crystals from the TXWC and TCG plutons have medium Th and

U contents: the TXWC titanite crystals contain 432 ppm Th and 151 ppm U while the TCG titanite crystals contain 395 ppm Th and 101 ppm U. Titanite crystals from the CXWC pluton have the lowest Th/U ratios among the four selected granite plutons. However, the whole-rock Th/U ratios of this pluton are not lower than those from the other plutons.

Ga-Sr-Cu-Mo

The contents of Ga, Sr, Cu, and Mo in titanite can be used to trace magmatic oxidation states, crystallization history and metal fertility. Thus, we investigated the variations in contents of these elements in titanite crystals. The abundances of Ga, Sr, Cu, and Mo in titanite from the four selected granite plutons show no correlation. The highest Ga content is detected in titanite from the TXWC pluton (59 ppm); medium Ga contents are observed in titanite from the PL pluton (50 ppm) and the TCG pluton (49 ppm); the lowest Ga content is found in titanite from the CXWC pluton (39 ppm). The highest Sr content is detected in titanite from the TCG pluton (77 ppm); medium Sr contents are found in titanite from the PL pluton (63 ppm) and the TXWC pluton (25 ppm); the lowest Sr content is observed in titanite from the CXWC pluton (12 ppm). The contents of Cu in titanite from the different plutons rarely exceed 1 ppm. The contents of Mo in the titanite crystals are much higher. The highest Mo content is detected in titanite from the CXWC pluton (104 ppm); medium Mo contents in titanite are observed in titanite from the TCG pluton (69 ppm) and the PL pluton (60 ppm): the lowest Mo content is found in titanite from the TXWC pluton (19 ppm).

The co-variation of the contents of REE, Y, Nb, Ta, Th, U, Ga, and Sr between whole rocks and titanite crystals can be seen in Fig. 6. The factors controlling these co-variations will be discussed below.

DOI: https://doi.org/10.2138/am-2018-6224

Trace elements in zircon

The contents of trace elements in zircon crystals have been shown in Table. 4. High Th/U ratios (>0.1）suggest the selected zircon crystals are igneous. The Ce and Ti contents in zircon from the CXWC, TCG, PL and TXWC plutons are 36.6 ppm, 41.5 ppm, 30.4 ppm, 70.9 ppm; and 4.30 ppm, 3.76 ppm, 4.85 ppm, 4.29ppm, respectively. We calculated the magmatic oxygen fugacity and temperatures using the method proposed by Trail et al. (2012) and Ferry and Watson (2007). The result (Table.4) shows that the parental magmas of these four plutons have similar temperature (720-742□). The parental magmas of the PL, TXWC, and TCG plutons have higher log (fO_2) = -10.4, -11.0, -13.3, respectively than CXWC pluton with log (fO_2) = -15.1.

Discussions

Origin of the analyzed titanite

The titanite crystals from these four plutons are interpreted as igneous for the following reasons. First, in terms of chemical compositions, the analyzed titanite crystals are clearly different from metamorphic and hydrothermal titanite crystals. The metamorphic and hydrothermal titanite crystals commonly have extremely low Th/U ratios close to zero, plus flat chondrite-normalized REE patterns or depletions in light REE relative to heavy REE (Aleinikoff et al. 2002; Chen et al. 2013; Papapavlou et al. 2017). The Al and Fe contents and Al/Fe ratios of the analyzed titanite from the four selected granite plutons are all similar to the values of typical igneous titanite in diorites and granites worldwide, such as low Al (0.02–0.06 awful), high Fe (0.03–0.06 awful) and low Al/Fe ratios(0.63–1.5) (Aleinikoff et al. 2002). High total REE contents (2340–8170 ppm), high HFSE contents such as Zr (174–463 ppm) and Nb (134–397 ppm) (Table 2), negative Eu anomalies and nearly flat heavy REE patterns for the analyzed titanite crystals from the four selected granite plutons (Fig. 7) provide further support for the magmatic origin, according to the genetic analysis for titanite by some previous studies (Xie et al. 2010; Gao et al. 2012; Jiang et al. 2016). Second, the interpretation of magmatic origin for the analyzed titanite based on chemical composition is consistent with textural observations. In all of the samples used in this study, titanite occurs as intergrowths with plagioclase, K-feldspar, hornblende and quartz that are not significantly altered (Fig. 8).

The analyzed titanite crystals can be further divided into early and late phases during granite crystallization. Those in the PL, TXWC and TCG plutons, which mostly have euhedral, elongated morphology and yellowish color, are interpreted to be early phases (Fig. 8d-i). Those in the CXWC pluton, which have anhedral morphology, contain apatite inclusions, and occur in the interstitial assemblages, are interpreted to be late phases (Fig. 8a-c). Our interpretations for the analyzed titanite crystals from the different plutons are consistent with higher F contents in those from the CXCW pluton than those from the other plutons. Previous studies have shown that F is capable of forming a complex with Ti, which hinders the removal of Ti from melts by incorporated into early crystal phases and results in a large amount of residual Ti in melt (Keppler 1993; Agangi et al. 2010). Thus the crystallization of titanite that contains Ti as essential structural constituents, as we see in the CXCW pluton, would be delayed due to the F-rich system.

Controls on titanite compositional variations

The chemical formula of titanite is $CaTi(SiO_4)O$. Without any substitution for Ca, the ideal CaO content in titanite is 28.6 wt.%. The contents of CaO in the analyzed titanite from the four selected granite plutons are all substantially lower than the ideal value, indicating significant substitution of Ca by other elements. The negative correlation between CaO and REE in titanite crystals (Fig. 5a) supports the reaction of $Ca^{2+} + Ti^{4+} = REE^{3+} + (Al, Fe^{3+})$, (1) is an important mechanism for Ca substitution (Franz and Spear 1985; Bernau and Franz 1987; Vuorinen and Halenius 2005). However, no correlation between CaO and TiO_2 is shown for titanite crystals from the CXWC pluton (Fig. 5b), implying that Ca substitution by REE or Ti substitution by Al plus Fe in these samples is more complicated than reaction (1).

Without any element substitution for Ti, the ideal TiO_2 content in titanite is 40.13 wt.%. The contents of TiO_2 in the analyzed titanite from the four selected granite plutons (33-37 wt.%) are all significantly lower than the ideal value. The positive correlation between CaO and TiO_2 (Fig. 5b) and negative correlation between TiO_2 and (Al_2O_3+Fe_2O_3) (Fig. 5c) for the titanite crystals from the TCG, PL and TXWC plutons (Fig. 5b) indicates that reaction (1) is an important mechanism for Ti substitution in these samples. The observed negative correlation between TiO_2 and (Al_2O_3+Fe_2O_3) (Fig. 5c) and positive correlation between F and (Al_2O_3+Fe_2O_3) (Fig.5d) in the CXWC titanite crystals suggests that the reaction of $Ti^{4+} + O^{2-} = (Al, Fe^{3+}) + (F, OH)^-$ (2) (Franz and Spear 1985; Bernau and Franz 1987; Enami et al. 1993; Carswell et al. 1996) is also significant for Ti substitution in these samples. However, the lack of correlation between CaO and TiO_2 (Fig. 5b) implies that reaction (1) is not very important for Ti substitution in these CXWC titanites probably due to this F-rich magma that favors reaction (2). In addition, the lack of correlation between (Nb+Ta) and TiO_2 (Fig. 5e) indicates that reaction of $2Ti^{4+} = (Nb+Ta^{5+}) + (Al, Fe^{3+})$ (3) (Franz and Spear 1985; Bernau and Franz 1987; Enami et al. 1993; Carswell et al. 1996) is negligible for Ti substitution in titanites.

The contents of SiO_2 in the analyzed titanite from the four selected granite plutons are ~30 wt.%, which are only slightly lower than the ideal value for titanite (30.65 wt.%) if no element substitution for Si occurs. The results show that element substitution for Si is indeed not important in the samples we analyzed.

Halogens (F and OH^-) in titanite occupy the underbonded O1 site, substituting O^{2-} *via* reaction (2) (Ribbe 1980; Oberti et al. 1991; Enami et al. 1993; Markl and Piazolo 1999; Troitzsch and Ellis 2002). The concentrations of F in titanite crystals from the TCG, PL and TXWC plutons are relatively low as compared to that in the titanite crystals from the CXWC pluton. This, together with the lack of correlation between F and (Al_2O_3+Fe_2O_3) for this mineral (Fig. 5d), indicates that such an exchange reaction is not important for these plutons. In contrast, titanite crystals from the CXWC pluton exhibit a positive correlation between F and (Al_2O_3+Fe_2O_3) (Fig. 5d) and a negative correlation between F and TiO_2 (Fig. 5f), indicating that this reaction is important for this pluton.

Some trace elements in titanite occupy either the heptahedral Ca site or the octahedral Ti site through isomorphous substitution. The former include Sr, REE, Y, Th and U (Higgens and Ribbe 1976; Deer et al. 1982), while the latter include Nb, Ta (Bernau and Franz 1987; Cérny et al. 1995; Knoche et al. 1998; Cempírek et al. 2008; Lucassen et al. 2011). Without the effects of subsolidus element exchange reactions, the contents of the trace elements in titanite are mainly controlled by their abundances in the parental magma and the titanite/magma partition coefficients that are strongly influenced by magma composition, oxygen fugacity, temperature and total pressure (Tiepolo et al. 2002; Prowatke and Klemme 2005; 2006; Anand and Balakrishnan 2011).

Based on their variations in titanite crystals and host rocks, the selected trace elements can be divided two groups. The first group of elements, such as Sr, and U, exhibit a positive correlation between them as well as between titanite and the host rocks (Fig. 6a; b), implying that these elements behave similarly in the various magmatic systems and that the whole rock and magma compositions are similar. The second group of elements, such as Y, REE, Nb, Ta and Th, do not show the positive correlation between titanite and the host rocks (Fig. 6c-g). This could be due to different bulk partition coefficients for different magmatic systems or simply because the whole rock and magma compositions are dramatically different. The dilemma of relatively high concentrations of Th and REE in whole rocks but low concentrations of these elements in titanite for the CXWC pluton (Fig. 6c; e) can be explained by the presence of allanite that crystallized before titanite and consumed large amounts of REE and Th from magma before titanite crystallization.

Magma differentiation and REE-Sr variations in titanite

The chondrite-normalized REE patterns of titanite crystals from the four selected granite plutons are slightly different (Fig. 7). Based on euhedral morphology, the titanite crystals from the TCG, PL and TXWC plutons were the early crystallizing phases. When titanite crystallized, the melt compositions were similar to the whole-rock compositions due to the lack of magmatic differentiation. Thus titanite crystals crystallizing from such melt could largely show the similar REE features with their host rocks. As a result, the higher $(La/Sm)_N$, $(La/Yb)_N$, $(Sm/Yb)_N$, and δEu are shown in titanite from the TCG pluton (0.76-2.2, 4.2-16.1, 4.2-9.4, 0.6-0.9 respectively) than that from the PL (0.6--2.9, 2.8-11.1, 3.8-6.4, 0.56-0.69 respectively) and TXWC plutons (0.5-0.9, 1.1-3.3, 1.7-5.9, 0.27-0.57 respectively), which is consistent with the higher these values in the TCG pluton than that in other plutons. Available experimental data show that under the same conditions, the partition coefficients for middle REE such as Sm between titanite and magma are higher than those for light REE such as La and heavy REE such as Yb (Green and Pearson 1986; Tiepolo et al. 2002; Prowatke and Klemme 2005; Olin and

Wolf 2012). Moreover, we have calculated the REE partition coefficients of titanite/melt through dividing the average content of each REE in titanite by those in the whole rock, assumed that the REE contents of the melt where titanite crystallized could be represented by those of the whole rock. The calculational results (Table. 3) also show that MREE partition coefficients of titanite/melt are higher than those of LREE and HREE. This explains the observation that titanite crystals from these plutons have lower $(La/Sm)_N$ and higher $(Sm/Yb)_N$ than the host rocks.

The variation of Sr contents in titanite commonly reflects magma compositional variation due to the crystallization of Sr-rich minerals such as plagioclase (Icenhower and London 1996; White et al. 2003; White 2003; Ren 2004; Xu et al. 2015). The abundances of Sr in titanite from the PL, TXWC and TCG plutons are highly variable (Fig. 9), which may have resulted from different timing during the course of associated plagioclase crystallization. In contrast, the low Sr contents in titanite from the CXWC pluton (Fig. 9) would imply the late-stage crystallization of titanite occurred after the massive crystallization of plagioclase. The more restricted range of Sr contents in these titanite crystals (Fig. 9) implies the crystallization of less plagioclase during titanite crystallization.

The co-variation between Sr contents and other components in titanite can be used to trace magmatic crystallization history. For example, our results have shown that the ratios of $(Sm/Yb)_N$ and $(La/Yb)_N$ decrease with the decrease of Sr contents in the titanite crystals (Fig. 9). Available experimental data indicate that under the same conditions the partition coefficients for middle REE such as Sm between allanite or apatite and magma are also higher than those for heavy REE such as Yb (Watson and Green 1981; Ayers and Watson 1993; Gieré and Sorenson 2004). As a result, the removal of these phases and plagioclase from melt will decrease $(Sm/Yb)_N$ and Sr contents in the fractionated melt. Consequently, titanite crystals crystallizing from the fractionated melt will also display the synchronous decrease in $(Sm/Yb)_N$ ratios and Sr contents (Fig. 9b). Lower $(Sm/Yb)_N$ ratios for titanite crystals from the CXWC pluton than those from the other three plutons are consistent with different timing of titanite crystallization revealed by textural variations. Lower $(Sm/Yb)_N$ ratios for titanite than the host rock samples from the CXWC pluton can be explained by the presence of significant amounts of early REE-rich minerals such as allanite and apatite.

Similarly, the $(La/Yb)_N$ variations in titanite crystals from the CXWC pluton (Fig. 9a) may be ascribable to the crystallization of allanite. Allanite as a very important carrier of La occurs in the CXWC pluton. Crystallization of this mineral from magma will decrease the $(La/Yb)_N$ ratio in the residual melt (Brooks et al. 1981; Frei et al. 2003; Gieré and Sorenson 2004). Another process that may decrease such ratio is the exsolution of Cl-rich fluid during magma fractional crystallization because the partition coefficients for light REE such as La are much higher than those for heavy REE such as Yb (Hass et al. 1995; Mayanovic et al. 2009). The relative significance of these two competing processes during the evolution of the studied magmatic system is yet to be determined. However, due to the lack of allanite in rock, the $(La/Yb)_N$ variations in titanite crystals from the TCG, PL, and TXWC plutons are more likely to be restricted by the second process.

Variation of Ga abundance, δCe and Fe_2O_3/Al_2O_3 in titanite with oxidation state

Fe_2O_3/Al_2O_3, δEu, δCe and Ga contents in titanite are sensitive to the oxidation state of the parental magma for titanite (King et al. 2013; Xu et al. 2015). Eu^{3+}, Ce^{3+}, Ga^{3+} and Fe^{3+} are favored by titanite, because Eu^{3+} and Ce^{3+} can occupy the heptahedral Ca site while Ga^{3+} and Fe^{3+} can occupy the octahedral Ti site (Frost et al. 2000; Tiepolo et al. 2002; King et al. 2013; Xu et al. 2015). The increased oxygen fugacity increases Eu^{3+}, Ce^{4+}, Ga^{3+} and Fe^{3+}

at the expense of Eu^{2+}, Ce^{3+}, Ga^{2+} and Fe^{2+} in magma, which facilitates the incorporation of more Eu, Ga, and Fe, but less Ce into titanite. As a result, titanite crystallizing from more oxidized magma will have higher Ga content, δEu and Fe_2O_3/Al_2O_3 but lower δCe than that crystallizing from more reduced magma if everything else in the magma remains the same. However, the decrease of δEu in titanite can also result from plagioclase crystallization from magma (Ballard et al. 2002; Bi et al. 2002; Buick et al. 2007; Xu et al. 2015). Thus, co-variation of two multi-variance elements is a better indicator for the change of oxidation state.

δEu and δCe in titanite crystals from the TXWC pluton are negatively correlated (Fig. 10a). The co-variation of these two indexes that are sensitive to the oxidation state, indicates that oxidation state was a major control on the concentration variations of these elements. In contrast, titanite crystals from the TCG, PL and CXWC plutons do not display such a correlation, indicating that other factors such as fractional crystallization may play a role on the variation of these two indexes. Thus the relative magmatic oxygen fugacity of these four plutons cannot be determined by δEu and δCe in titanite crystals. As shown in Fig. 10b, δCe and the contents of Ga in titanite crystals from the CXWC and TCG plutons show a negative correlation. Such co-variations, together with higher Ga contents and lower δCe in titanite crystals from TCG plutons than that from CXWC pluton support the premise that the parental magma for the TCG pluton is more oxidized than that for the CXWC pluton. Moreover, a positive correlation between Ga contents and Fe_2O_3/Al_2O_3 ratios in the titanite crystals from the same two plutons can be observed (Fig. 10c). This, together with the more variable of contents of Ga and Fe_2O_3/Al_2O_3 ratios reveals the higher oxygen fugacity in the parental magma for the TCG pluton as well.

In order to verify above findings, we calculated the magmatic oxygen

DOI: https://doi.org/10.2138/am-2018-6224

fugacity by zircon Ce data. The result shows that the parental magma of the TCG pluton characterized by log(fO_2) =-13.3 is more oxidized than that of the CXWC pluton characterized by log(fO_2) =-15.1 under similar temperatures (720-732□) (Table.4). The consistent variations of log(fO_2) with titanite Ga contents (Fig. 11a) and Fe_2O_3/Al_2O_3 ratios (Fig. 11b) further support the conclusion. The difference in magmatic oxidation state between these two intracontinental granites is probably attributable to the magma source of the TCG pluton modified by the subduction-related fluids (Meng 2014).

Mo in titanite as an indicator of metal fertility for granites

In porphyry Cu and Mo deposits, due to the stockwork and disseminated style of mineralization, whole-rock samples may be mixed with the hydrothermal molybdenite and chalcopyrite, which inevitably causes the overestimation of Mo and Cu contents in the parental magma using whole rocks. Thus the metal contents in minerals instead of that in whole rocks, could be a better indicator for the variation of such metal contents in the parental magmas as long as the distribution coefficients for the metals of interest are relatively high. However, low distribution coefficients would make the metal contents in titanite insensitive to the content variations of these metal elements in magmas. For example, our data show that the contents of Cu are very low in titanite from all of the four selected granite plutons. Titanite crystals from the Cu-mineralized PL pluton do not have higher Cu contents (0.60-0.84 ppm) than those from the other plutons that are not Cu-mineralized (0.58-0.86 ppm). In contrast, titanite crystals have relatively higher Mo contents. Mo contents in titanite can be strictly controlled by the crystallization of molybdenite from magma, but molybdenite is considered a very uncommon magmatic phase with the occurrence reported in few plutons such as the peralkaline rhyolites from Pantelleria, Italy (Lowenstern et al. 1993; Lerchbaumer and Aud tat

2013). Although there are other magmas could saturate in molybdenite, we may not see it preserved since magmas oxidize a bit upon decompression and eruption due to degassing of H_2 (Mercer et al. 2015).

Audėtat et al (2011) counted the chemical compositions of several molybdenite-saturated plutons worldwide to identify the region of molybdenite-saturated plutons in the tectonic discrimination diagrams of Pearce (1984). Their results showed that the molybdenite is most likely to crystallize directly from relatively reduced magmas (mostly around QFM buffer) (Fig. 12) in the within-plate setting such as a continental rift (Fig. 13). According to the characteristics of trace elements (Rb, Nb, Y) in whole rock, the PL and TXWC plutons are considered to be subduction-related I-type granites (Fig. 13). Some samples of the TCG pluton show the compositional similarity to subduction-related granites, which is probably ascribable to its magma source influenced by pre-existing subduction-related material (Meng 2014). The CXWC pluton has been proved to be highly fractionated I-type granite. Thus some samples show the similar chemical characteristics to A- and S- type granite due to highly magmatic evolution (Fig. 13) (Wang et al. 2014b). Generally, samples from the PL, TXWC and TCG plutons all deviate from the region of the molybdenite-saturated plutons in the tectonic discrimination diagrams of Pearce (1984) proposed by Audėtat et al (2011). The estimated oxidation states of these magmatic systems are above the NNO buffer (Fig. 12a), indicating that molybdenite could not have crystallized directly from the parental magma for these plutons regardless of Mo concentration. Some samples from the CXWC pluton plot in the molybdenite-saturated region (Fig. 12; 13). However, the parental magma of this pluton is too oxidized (estimated to be around the NNO buffer, Fig. 12a) for molybdenite to crystallize directly from such a magma (Audėtat et al. 2011). These authors have shown that under fS_2 at the value corresponding to the assemblage pyrrhotite-magnetite-fayalite, the concentrations of 100-1000ppm

Mo in magma are needed for molybdenite to crystallize directly from the magma (Fig. 12b). These values are 2-3 orders of magnitude higher than the whole-rock Mo contents of the CXWC pluton (<10 ppm).

Titanite crystals from the TCG and PL plutons have similar Mo content (Fig. 14a), but the TCG pluton occurs with much more significant Mo mineralization than does the PL pluton. This discrepancy is discussed in the following section. Although economic-Mo mineralization all occurs in the TCG and CXWC plutons, higher Mo contents in titanite crystals from the CXWC pluton than those from the TCG pluton may have in part resulted from different oxidation states. Mo has two common valences, Mo^{5+} and Mo^{6+}. Mo^{5+} is more prone than Mo^{6+} to enter titanite through the following substitution reaction.

$$2Ti^{4+} = Mo^{5+} + (Al, Fe^{3+}). \qquad (4)$$

The negative correlation between Mo and TiO_2 for the samples (Fig. 14a) may have resulted from such an exchange reaction. This reaction can proceed more easily in more reduced magmatic system such as that of the CXWC pluton. As described above, the magma of the TCG pluton was more oxidized than that of the CXWC pluton. Another possible effect is the concentration of Mo in magma. Mo is an incompatible element during the crystallization of major minerals from felsic magma and may progressively become more enriched in residual magma as crystallization proceeds. But Mo in the titanite crystals from the CXWC pluton do not show this incompatible behavior with progressive crystallization (increasing Mo with decreasing Sr) (Fig. 14b), implying that Mo was not enriched in the residual melt.

Generally, in view of the difficulty of direct crystallization of molybdenite from the felsic magmas, titanite Mo contents thus would be a potential indicator for Mo fertile of different magmas if there is no significant difference in magmatic oxidation states.

Titanite as a metallogenic indicator for Mo deposits

Although the transference of metals from a magma to an ore deposit is a complex process, the popular hypothesis is that the metal-rich magmas are in favor of magma-related mineralization (Candela 1992; Richards 2015). However, it is still controversial that whether the mineralized-magmas must be extremely enriched with metal elements (Lerchbaumer and Audétat 2013; Zhang and Audétat 2016). The results from our study indicate that unusually high concentration of Mo in magmas is not very relevant to Mo mineralization, at least for the parental magmas of plutons that we have investigated. For example, titanite crystals from the Mo-economic TCG pluton (porphyry type) and the Mo-subeconomic PL pluton (porphyry type, Cu-dominant) have similar Mo contents (Fig. 14a). Considering more-reduced parental magma for the TCG (Fig. 12a), the Mo content in the parental magma for the TCG pluton could be in fact even lower than that in the parental magma for the PL pluton. Combined with slightly different whole-rock Mo contents between these two plutons, the Mo abundances in the parental magmas for these two plutons with different degrees of porphyry-style Mo mineralization may not be significantly different.

As mentioned above, feldspar crystallization in felsic magma can cause depletion of Sr in the residual melt, thereby producing Sr-depleted titanite crystallizing from such a melt. Thus if the oxidation state did not drastically change, the increasing Mo contents with decreasing Sr contents in titanite crystals from the TCG pluton (with porphyry Mo mineralization) could reflect the Mo enrichment in this residual melt. However, such a trend is not present in titanite crystals from the CXWC pluton (with Qz-vein type Mo mineralization) (Fig. 14b), implying that Mo enrichment in the residual melt by feldspar fractionation is not a prerequisite for Mo mineralization, at least not for the

Qz-vein type mineralization. In addition, although the control mechanism has not been identified, a drastic variation of Mo contents (101-154 ppm) within a limited range of Sr contents (9.62-12.63 ppm) that is observed in some CXWC titanite crystals from the biotite granite zone (Fig. 14b) may imply the possible heterogeneity of Mo distribution in this F-rich magma or one kind of non-equilibrium incorporation of Mo into the titanite occurring in such a magma system.

Our results are generally consistent with the previous findings from Lerchbaumer and Audėtat (2013). These authors studied melt inclusions from three sub-economically Mo mineralized granites in USA and Norway that all record a clear trend of increasing Mo concentrations with increasing degree of melt differentiation. Moreover, by comparing Mo/Cs ratios of melt inclusion from the intrusions related to the porphyry Mo and Cu deposits, and barren intrusions, they found that most subduction-related magmas have lower Mo/Cs ratios than within-plate magmas, but that within these two groups, there are no systematic differences between barren and productive intrusions. Based on these findings, they suggested that the mineralization potential of Mo is not primarily controlled by the contents of Mo in the melts, but rather by other factors such as size of the magma chamber and the efficiency of residual melt and fluid extraction from the magma chamber and their focusing into a small apophysis at its top. They also suggested that the formation of crystal-poor melts at the top of the magma chamber, and the development of convection cells are essential for Mo granite-related mineralization. However, due to high viscosity of felsic magma with high SiO_2 contents, these two processes may be hindered. Therefore, the volatile components (F, Cl, H_2O) that lead to the decrease in magmatic viscosity and facilitate the melt extraction from the crystal mush are very important for Mo mineralization (e.g., Mercer et al. 2015). Among these volatile components, F could be more efficient because previous studies have shown compared to Cl and H_2O, F tends to residue in magma

(Candela 1986; Warner et al. 1998). In addition, F concentrations in the residual melt could be effective for enhancing the solubility of H_2O and Cl in melt, which causes the further decrease of magmatic viscosity (Webster and Holloway 1990; Holtz et al. 1993). As a result, it follows that F-rich felsic magmas may create relatively high potential for Mo mineralization (e.g., Gunow et al. 1980; Webb et al. 1992), especially in the within-plated magmas that generally lack H_2O and Cl compared to the arc magmas.

The significance of high F concentrations in felsic magmas to facilitate Mo mineralization is also evident from this study, although the detailed mechanisms are still unclear. We have found that titanite crystals from the two Mo-mineralized granite plutons (CXWC and TCG) are all F-rich. Overall, those from the CXWC pluton tend to have higher F contents than those from the TCG pluton. Considering the loss of F during late-stage magmatic degassing (Wallace et al. 2015), the whole-rock samples cannot fully record the F characteristics of the magma. Thus if absence of melt inclusion data, the variation of F in titanite may be used to assist in the exploration of Mo ore deposits. In light of the fact that high Mo abundances in melts are not the only requirements to form granite-related Mo deposits, relying solely on Mo concentration in titanite is far from enough to be a predictor of economic Mo mineralization. Other factors such as magmatic volatile components especially F and oxidation state also revealed by titanite chemistry are indispensable. For example, our data show that titanite crystals from the Mo-mineralized and non-mineralized rocks we have studied are different in the index system consisting of titanite F and Mo contents, and Fe_2O_3/Al_2O_3 ratios (Fig. 15). We show that the granites containing titanite crystals with the average contents of Mo (>50 ppm), F contents (>0.30 wt.%) and Fe_2O_3/Al_2O_3 ratios (<1.5) have high potential for economic Mo mineralization. However, more data are still need to evaluate the effectiveness of such exploration tool in future work.

Conclusions and implications

The results from this study confirm that titanite is a good petrogenetic-metallogenic indicator. The Ga abundance and some element ratios such as δEu, δCe and Fe_2O_3/Al_2O_3 in titanite are good indicators for the oxidation state of the parental magma. The concentrations of Mo, Sr, REE, and F in titanite mainly reflect magma compositions and crystallization history. Specifically, titanite crystals from several plutons with different extents of Mo mineralization have similar Mo contents and do not always exhibit a negative correlation between Mo and Sr abundances (indicating continuous enrichment of Mo in residual melt due to fractional crystallization). The results from this study are consistent with the previous findings that high initial Mo contents in the parental magma and its residual enrichment by fractional crystallization are not the only requirements to form a granite-related Mo ore deposit (Lerchbaumer and Audėtat 2013). As suggested by these authors, other processes such as efficient separation of residual melt and associated fluid extraction, possibly facilitated by high F content in the magma, are also important. The significance of high F concentration in magma to facilitate Mo mineralization is indicated by the presence of F-rich titanite crystals in the two Mo-mineralized granite plutons (CXWC and TCG) that are included in this study. In view of above findings, we believe that a future attempt to use titanite Mo concentrations as a predictor for economic Mo deposits is inadequate to rely on but combined with other crucial factors such as magmatic volatile components and oxidation state revealed by titanite F contents and Fe_2O_3/Al_2O_3 ratios. Such an approach to evaluating the metallogenic potential of granites is reasonable.

Our study provides a successful example to illustrate the advantages of using titanite compositions to track some magma physical and chemical properties such as magmatic crystallizing history, oxidation state and ore potential that the whole-rock composition cannot effectively reveal. Clearly, titanite chemistry has many advantages over whole-rock chemistry in the study of the genetic relationship between magma evolution and metallogeny. There is no doubt that titanite in situ composition as a better petrogenetic and metallogenic indicator than whole-rock composition has great application potential in petrology and petrogeochemistry.

Acknowledgements

This study was supported by the Strategic Priority Research Program (B) of the Chinese Academy of Sciences (XDB18000000), the National Natural Science Foundation of China (Grants41703050), the CAS/SAFEA international Partnership Program for Creative Research Teams-(Intraplate Mineralization Research Team; KZZD-EW-TZ-20) and the national Key R&D Program of China (2016YFC0600503). We thank Ms. Zhi-Hui Dai and Chong-Yin Li for their assistance in titanite trace element analysis by LA-ICP-MS, Ms. Wen-Qin Zheng for her assistance in titanite chemical analysis by EPMA, and Ms. Jing Hu and Guang-Ping Bao for their assistance in whole-rock chemical analysis by XRF and ICP-MS. Comments from the reviewers and detailed revision guidance from Associate Editor Dr. Celestine Mercer are greatly appreciated.

References

Agangi, A., Kamenetsky, V.S., and McPhie, J. (2010) The role of fluorine in the concentration and transport of lithophile trace elements in felsic magmas: insights from the Gawler Range Volcanics, South Australia. Chemical Geology, 273, 314-325.

DOI: https://doi.org/10.2138/am-2018-6224

Aleinikoff, J.N., Wintsch, R.P., Fanning, C.M., and Dorais, M.J. (2002) U-Pb geochronology of zircon and polygenetic titanite from the Glastonbury Complex, Connecticut, USA: an integrated SEM, EMPA, TIMS, and SHRIMP study. Chemical Geology, 188, 125-147.

Aleksandrov, S.M. and Troneva, M.A. (2007) Composition, mineral assemblages, and genesis of titanite and malayaite in skarns. Geochemistry International, 45, 1012-1024.

Anand, R. and Balakrishman, S. (2011) Geochemical and Sm-Nd isotopic study of titanite from granitoid rocks of the eastern Dharwar craton, southern India. Journal of Earth System Science, 120, 237-251.

Audėtat, A., Dolejš, D., and Lowenstern, J.B. (2011) Molybdenite saturation in silicic magmas: occurrence and petrological implications. Journal of Petrology, 52, 891-904.

Ayers, J.C. and Watson, E.B. (1993) Apatite/fluid partitioning of rare earth elements and strontium: experimental results at 1.0 GPa and 1000°C and application to models of fluid–rock interaction. Chemical Geology 110, 299-314.

Bachmann, O., Dungan, M.A., and Bussy, F. (2005) Insights into shallow magmatic processes in large silicic magma bodies: the trace element record in the Fish Canyon magma body, Colorado. Contributions to

Mineralogy and Petrology, 43, 1469-1503.

Ballard, J.R., Palin, J.M., and Campbell, I.H. (2002) Relative oxidation states of magmas inferred from Ce(IV)/Ce(III) in zircon: application to porphyry copper deposits of northern Chile. Contributions to Mineralogy and Petrology, 144, 347-364.

Bernau, V.R. and Franz, G. (1987) Crystal chemistry and genesis of Nb-, V- and Al- rich metamorphic titanite from Egypt and Greece. The Canadian Mineralogist, 25, 695-705.

Bi, X.W., Cornell, D.H., and Hu, R.Z. (2002) REE composition of primary and altered feldspar from the mineralized alteration zone of alkali-rich intrusive rocks, Western Yunnan Province, China. Ore Geology Reviews, 19, 69-78.

Brooks, C.K., Henderson, P., and Ronsbo, J.G. (1981) Rare-earth partition between allanite and glass in the obsidian of Sandy Braes, Northern Ireland. Mineralogical Magazine, 44, 157-160.

Bruand, E., Storey, C., and Fowler, M. (2014) Accessory mineral chemistry of high Ba-Sr granites from northern Scotland: constraints on petrogenesis and records of whole-rock signature. Journal of Petrology, 55, 1619-1651.

Buick, I.S., Hermann, J., Mass, R., and Gibson, R.L. (2007) The timing of

DOI: https://doi.org/10.2138/am-2018-6224

subsolidus hydrothermal alteration in the Central Zone, Limpopo Belt (South Africa): constraints from titanite U-Pb geochronology and REE partitioning. Lithos, 98, 97-117.

Candela, P.A. (1986) Toward a thermodynamic model for the halogens in magmatic systems: An application to melt-vapor-apatite equilibria. Chemical Geology, 57, 289-301.

Candela, P.A. (1992) Controls on ore metal ratios in granite-related ore systems: an experimental and computational approach. Transactions of the Royal Society of Edinburgh Earth Sciences, 83, 317-326.

Carmichael, I.S.E. and Nicholls, J. (1967) Iron-titanium oxides and oxygen fugacities in volcanic rocks. Journal of Geophysical Research, 72, 4665-4687.

Carswell, D.A., Wilson, R.N., and Zhai, M. (1996) Ultra-high pressure aluminous titanite in carbonate-bearing eclogites at Ahuanghe in Dabieshan, central China. Mineralogical Magazine, 60, 461-471.

Cempírek, J., Houzar, S., and Novák, M. (2008) Complexly zoned niobian titanite from hedenbergite skarn at Písek, Czech Republic, constrained by substitutions Al(Nb,Ta)Ti_{-2}, Al(F,OH)$(TiO)_{-1}$ and $SnTi_{-1}$. Mineralogical Magazine, 72, 1293-1305.

Cérny, P., Novák, M., and Chapman, R. (1995) The Al(Nb,Ta)Ti(in-2) substitution in titanite: the emergence of a new species? Mineralogy and Petrology, 52, 61-73.

Che, X.D., Linnen, R.L., Wang, R.C., Groat, L.A., and Brand, A.A. (2013) Distribution of trace and rare earth elements in titanite from tungsten and molybdenum deposits in Yukon and British Columbia, Canada. The Canadian Mineralogist, 51, 415-438.

Chen, Y.X., Zheng, Y.F., and Hu, Z.C. (2013) Polyphase growth of accessory minerals during continental collision: geochemical evidence from ultrahigh-preesure metamophic gneisses in the Sulu orogen. Lithos, 177, 245-267.

Corfu, F. and Muir, T. (1989) The Hemlo-Heron Bay greenstone belt and Hemlo Au-Mo deposit, Superior Province, Ontario, Canada 2. Timing of metamorphism, alteration and Au mineralization from titanite, rutile, and monazite U-Pb geochronology. Chemical Geology, 79, 201-223

Deer, W.A., Howie, R.A., and Zussman, J. (1982) Rock forming minerals. Orthosilicates, 1A. Longman, London.

Enami, M., Suzuki, K., Liou, J.G., and Bird, D.K. (1993) Al-Fe^{3+} and F-OH substitutions in titanite and constraints on their P-T dependence. European Journal of Mineralogy, 5, 219-231.

Essex, R.M. and Gromet, L.P. (2000) U-Pb dating of prograde and retrograde titanite growth during the Scandian Orogeny. Geology, 28, 419-422.

Ferry, M. and Watson, E.B. (2007) New thermodynamic models and revised calibrations for Ti-in-zircon and Zr-in-rutile thermometers. Contributions to Mineralogy and Petrology, 154, 429-437.

Franz, G. and Spear, F.S. (1985) Aluminous titanite (sphene) from the eclogite zone, south-central Tauern Window, Austria. Chemical Geology, 50, 33-46.

Frei, D., Liebscher, A., Wittenberg, A., and Shaw, C.S.L. (2003) Crystal chemical controls on rare earth element partitioning between epidote-group minerals and melts: an experimental and theoretical study. Contributions to Mineralogy and Petrology, 146, 192-204.

Frost, B.R., Chamberlain, K.R., and Schumacher, J.C. (2000) Sphene (titanite): Phase relations and role as a geochronometer. Chemical Geology, 172, 131-148.

Gao, X.Y., Zheng, Y.F., Chen, Y.X., and Guo, J.L. (2012) Geochemical and U-Pb age constraints on the occurrence of polygenetic titanite in UHP metagranite in the Dabie orogen. Lithos, 136-139, 93-108.

Gieré, R. and Sorensen, S. (2004) Allanite and other REE-rich epidote-group minerals. Reviews in Mineralogy and Geochemistry, 56, 431-493.

Glazner, A.F., Coleman, D.S., and Bartley, J.M. (2008) The tenuous connection between high-silica rhyolites and granodiorite plutons. Geology, 36, 183-186.

Green, T.H. and Pearson, N.J. (1986) Rare-earth element partitioning between sphene and coexisting silicate liquid at high-pressure and temperature. Chemical Geology, 55, 105-119.

Gunow, A.J., Ludington, S., and Munoz, J.L. (1980) Fluorine in micas from the Henderson molybdenite deposit, Colorado. Society of Economic Geologists, Inc. Economic Geology, 75, 1127-1137.

Haas, J.R., Shock, E.L., and Sassani, D.C. (1995) Rare earth elements in hydrothermal systems: Estimates of standard partial molal thermodynamic properties of aqueous complexes of the rare earth elements at high pressures and temperatures. Geochimica et Cosmochimica Acta, 59, 4329-4350.

Hayden, L., Watson, E.B., and Wark, D.A. (2008) A thermobarometer for sphene (titanite). Contributions to Mineralogy and Petrology, 155, 529-540.

Higgins, J.B. and Ribbe, P.H. (1976) The crystal chemistry and space groups of natural and synthetic titanites. American mineralogist, 61, 878-888.

Holtz, F., Digwell, D.B., and Behrens, H. (1993) Effect of F, B_2O_3 and P_2O_5 on the solubility of water in haplogranite melt compared to natural silicate

This is a preprint, the final version is subject to change, of the American Mineralogist (MSA)
Cite as Authors (Year) Title. American Mineralogist, in press.
DOI: https://doi.org/10.2138/am-2018-6224

melts. Contribution to Mineralogy and Petrology, 113, 492-501.

Hou, Z.Q. (1993) Tectono-magmatic evolution of the Yidun Island- arc and geodynamic setting of Kuroko-type sulfide deposits in Sanjiang region, China. Resource Geology (Special Issue), 17, 336-357.

Icenhower, J. and London, D. (1996) Experimental partitioning of Rb, Cs, Sr, and Ba between alkali feldspar and peraluminous melt. American Mineralogist, 81, 719-734.

Jiang, P., Yang, K.F., Fan, H.R., Liu, X., Cai, Y.C., and Yang, Y.H. (2016) Titanite-scale insight into multi-stage magma mixing in Early Cretaceous of NW Jiaodong terrane, North China Craton. Lithos, 258-259, 197-214.

Knoche, R., Angel, R.J., Seifert, F., and Fliervoet, T.F. (1998) Complete substitution of Si for Ti in titanite $Ca(Ti_{1-x}Si_x)^{VI}Si^{IV}O_5$. American Mineralogist, 83, 1168-1175.

Keppler, H. (1993) Influence of fluorine on the enrichment of high field strength trace elements in granitic rocks. Contributions to Mineralogy and Petrology, 114, 479-488.

King, P.L., Sham, T.K., Gordon, R.A., and Dyar, M.D. (2013) Microbeam X-ray analysis of Ce^{3+}/Ce^{4+} in Ti-rich minerals: A case study with titanite (sphene) with implications for multivalent trace element substitution in minerals. American Mineralogist, 98, 110-119.

Leng, C.B., Huang, Q.Y., Zhang, X.C., Wang, S.X., Zhong, H., Hu, R.Z., Bi, X.W., Zhu, J.J., and Wang, X.S. (2014) Petrogenesis of the Late Triassic volcanic rocks in the Southern Yidun arc, SW China: Constraints from the geochronology, geochemistry, and Sr-Nd-Pb-Hf isotopes. Lithos, 190-191, 363-382.

Lerchbaumer, L. and Audėtat, A. (2013) The metal content of silicate melts and aqueous fluids in subeconomically Mo mineralized granites: implications for porphyry Mo genesis. Economic Geology, 108, 987-1013.

Li, J.K., Li, W.C., Wang, D.H., Lu, Y.X., Yin, G.H., and Xue, S.R. (2007) Re-Os dating for ore-forming event in the late of Yanshan Epoch and research of ore-forming regularity in Zhongdian arc. Acta Petrologica Sinica, 23, 2415–2422.

Li, J.W., Deng, X.D., Zhou, M.F., Liu, Y.S., Zhao, X.F., and Guo, J.L. (2010) Laser ablation ICP-MS titanite U-TH-Pb dating of hydrothermal ore deposits: A case study of the Tonglushan Cu-Fe-Au skarn deposit, SE Hubei Province,China. Chemical Geology, 270, 56-67.

Li, W.C. (2007) The Tectonic Evolution of the Yidun Island Arc and the Metallogenic Modelof the Pulang Porphyry Copper Deposit, Yunnan

SW China. (PhD Thesis) China University of Geosciences, (Beijing).

Li, W.C., Yin, G.H., Yu, H.J., and Liu, X.L. (2014) The Yanshanian granites and associated Mo polymetallic mineralization in the Xiangcheng-Luoji area of the Sanjiang-Yangtze conjunction zone in Southwest China. Acta Geologica Sinica-English Edition, 88, 1742-1756.

Liferovich, R. and Mitchell, R.H. (2005) Composition and paragenesis of Na-, Nb-, and Zr- bearing titanite from Khibina, Russia, and crystal-structure data for synthetic analogues. The Canadian Mineralogist, 43, 795-812.

Liu, Y.S., Hu, Z.C., Gao, S., Gunther, D., Xu, J., Gao, C.G., and Chen, H.H. (2008) In situ analysis of major and trace elements of anhydrous minerals by LA-ICP-MS without applying an internal standard. Chemical Geology, 257, 34-43.

Liu, X.L., Li, W.C., Yang, F.C., Zhang, N., Yan, T.L., and Luo, Y. (2017) Zircon U-Pb age and Hf isotopic composition of the two-period magmatism of the Xiuwacu Mo-W-Cu deposit in the Geza arc belt, Yunnan and their tectonic significance. Acta Geologica Sinica, 91, 849-863.

Lowenstern, J.B., Mahood, G.A., Hervig, R.L., and Sparks, J. (1993) The occurrence and distribution of Mo and molybdenite in un-altered peralkaline rhyolites from Pantelleria, Italy. Contributions to Mineralogy and Petrology, 114,119-129.

Lucassen, F., Franz, G., Dulski, P., Romer, R.L., and Rhede, D. (2011) Element and Sr isotope signature of titanite as indicator of variable fluid composition in hydrated eclogite. Lithos, 121, 12-24.

Maniar, P.D. and Piccoli P.M. (1989) Tectonic discrimination of granitoids. Bulletin of the Geological Society of America, 101, 635.

Markl, G. and Piazolo, S. (1999) Stability of high-Al titanite from low-pressure calc-silicates in light of fluid and host rock composition. American Mineralogist, 84, 37-47.

Marks, M.A.W., Coulson, I.M., Schilling, J., Dorrit, E.J., Schmitt, A.K., and Markl, G. (2008) The effect of titanite and other HFSE-rich mineral (Ti-bearing andradite, zircon, eudialyte) fractionation on the geochemical evolution of silicate melts. Chemical Geology, 257, 153–172.

Mayanovic, R.A., Anderson, A.J., Bassett, W.A., and Chou, I.M. (2009) Steric hindrance and the enhanced stability of light rare-earth elements in hydrothermal fluids. American Mineralogist, 94, 1487-1490.

Meng, J.Y. (2014) The porphyry copper-polymetallic deposit in Zhongdian, West Yunnan: magmatism and mineralization. (PhD Thesis) China University of Geosciences, (Beijing).

Mercer, C.N., Hofstra, A.H., Todorov, T.I., Julie Roberge, J., Burgisser, A., Adams, D.T., and Cosca, M. (2015) Pre-Eruptive Conditions of the Hideaway Park Topaz Rhyolite: Insights into Metal Source and Evolution of Magma Parental to the Henderson Porphyry Molybdenum Deposit, Colorado. Journal of Petrology, 56, 645- 679.

Middlemost, E.A.K. (1994) Naming materials in the magma/igneous rock system. Earth-Science Reviews, 37, 215-224.

Nakada, S. (1991) Magmatic processes in titanite-bearing dacites, central Andes of Chile and Bolivia. American Mineralogist, 76, 548-560.

Oberti, R., Smith, D.C., Rossi, G., and Caucia, F. (1991) The crystal chemistry of high aluminium titanites. European Journal of Mineralogy, 3, 777-792.

Olin, P.H. and Wolff, J.A. (2012) Partitioning of rare earth and high field strength elements between titanite and phonolitic liquid. Lithos, 128-131, 46-54.

Pang, Z.S., Du, Y.S., Cao, Y., Gao, F.P., Wang, G.W., and Dong, Q. (2014) Geochemistry and zircon U-Pb geochronology of the Pulang Complex, Yunnan Province. China. Journal of Earth System Science, 123, 875-885.

Papapavlou, K., Darling, J.R., Storey, C.D., Lightfoot, P.C., Moser, D.E., and Lasallea, S. (2017) Dating shear zones with plastically deformed titanite: New insights into the orogenic evolution of the Sudbury impact structure (Ontario, Canada). Precambrian Research, 291, 220-235.

DOI: https://doi.org/10.2138/am-2018-6224

Pearce, J.A., Harris, N.B.W. and Tindle, A.G. (1984) Trace element discrimination diagrams for the tectonic interpretation of granitic rocks. Journal of Petrology, 25, 956-983.

Peng, T.P., Zhao, G.H., Fan, W.M., Peng, B.X., and Mao, Y.H. (2015) Late Triassic granitic magmatism in the Eastern Qiangtang, Eastern Tibetan Plateau: Geochronology, petrogenesis and implications for the tectonic evolution of the Paleo-Tethys. Gondwana Research, 27, 1494-1508.

Piccoli, P., Candela, P., and Rivers, M. (2000) Interpreting magmatic processes from accessory phases: titanite-a small-scale recorder of large-scale processes. Transactions of the Royal Society of Edinburgh, Earth Sciences, 91, 257-267.

Pidgeon, R.T., Bosch, D., and Bruguier, O. (1996) Inherited zircon and titanite O-Pb in Archean syenite from southwestern Australia: Implications for U-Pb stability of titanite. Earth and Planetary Science Letters, 141, 187-198.

Prowatke, S. and Klemme, S. (2005) Effect of melt composition on the partitioning of trace elements between titanite and silicate melt. Geochimica et Cosmochimica Acta, 69, 695-709.

Prowatke, S. and Klemme, S. (2006) Rare earth element partitioning between titanite and silicate melts: Henry's law revisited. Geochimica et

Cosmochimica Acta, 70, 4997-5012.

Qi, L., Hu, J., and Gregoire, D.C. (2000) Determination of trace elements in granites by inductively coupled plasma mass spectrometry. Talanta, 51, 507-513.

Ren, M.H. (2004) Partitioning of Sr, Ba, Rb, Y, and LREE between alkali feldspar and peraluminous silicic magma. American Mineralogist, 89, 1290-1303.

Ribbe, P.H. (1980) Titanite. Reviews in Mineralogy & Geochemistry, 5, 137-154.

Richards, J.P. (2015) The oxidation state, and sulfur and Cu contents of arc magmas: implications for metallogeny. Lithos, 233, 27-45.

Selvig, L.K., Inn, K.G.W., Outola, I.M.J., Kurosaki, H., and Lee, K.A. (2005) Dissolution of resistate minerals containing uranium and thorium: Environmental implications. Journal of Radioanalytical and Nuclear Chemistry, 263, 341-348.

Sun, S.S. and McDonough, W.F. (1989) Chemical and isotopic systematics of oceanic basalts: implications for mantle composition and processes. Geological Society Special Publication, 42, 313–345.

Tiepolo, M., Vannucci, R., Oberti, R., Foley, S., Bottazzi, P., and Zanetti, A. (2000) Nb and Ta incorporation and fractionation in titanian pargasite and kaersutite: crystal-chemical constraints and implications for natural systems. Earth and Planetary Science Letters, 176, 185-201.

Tiepolo, M., Oberti, R., and Vannucci, R. (2002) Trace element incorporation in titanite: constraints from experimentally determined solid/liquid partition coefficients. Chemical Geology, 191, 105-119.

Trail, D., Watson, E.B., and Tailby, N.D. (2012) Ce and Eu anomalies in zircon as proxies for the oxidation stateof magmas. Geochimica et Cosmochimica Acta, 97, 70-87.

Troitzsch, U. and Ellis, D.J. (2002) Thermodynamic properties and stability of AlF-bearing titanite $CaTiSiO_5$-$CaAlFSiO_4$. Contributions to Mineralogy and Petrology, 142, 543-563.

Tropper, P. and Manning, C.E. (2008) The current status of titanite-rutile thermobarometry in ultrahigh-pressure metamorphic rocks: The influence of titanite activity models on phase equilibrium calculations. Chemical Geology, 254, 123-132.

Tu, X.L., Zhang, H., Deng, W.F., Ling, M.X., Liang, H.Y., Liu, Y., and Sun, W.D. (2011) Application for RESOlution in-situ laser ablation ICP-MS in trace element analyses. Geochimica, 40, 83–98.

Vuorinen, J.H. and Halenius, U. (2005) Nb-, Zr- and LREE-rich titanite from the Alnö alkaline complex: crystal chemistry and its importance as petrogenetic indicator. Lithos, 83, 128-142.

Wallace P. J., Plank T., Edmonds M., and Hauri E.H. (2015) Chapter 7 volatiles in magmas. The Encyclopedia of Volcanoes, 163-183.

Wang, R.C., Xie, L., Chen, L., Yu, A.P., Wang, L.B., Lu, J.J., and Zhu, J.C. (2013) Tin-carrier minerals in metaluminous granites of the western Nanling Range (southern China): Constraints on processes of tin mineralization in oxidized granite. Journal of Asian Earth Sciences, 74, 361-372

Wang, B.Q., Zhou, M.F., Li, J.W., and Yan, D.P. (2011) Late Triassic porphyritic intrusions and associated volcanic rocks from the Shangri-La region, Yidun terrane, Eastern Tibetan Plateau: adakitic magmatism and porphyry copper mineralization. Lithos, 127, 24–38.

Wang, X.S., Bi, X.W., Leng, C.B., Zhong, H., Tang, H.F., Chen, Y.W., Yin, G.H., Huang, D.Z., and Zhou, M.F. (2014a) Geochronology and geochemistry of Late Cretaceous igneous intrusions and Mo-Cu-(W) mineralization in the southern Yidun arc, SW China: implications for metallogenesis and geodynamic setting. Ore Geology Reviews, 61, 73-95.

Wang, X.S., Hu, R.Z., Bi, X.W., Leng, C.B., Pan, L.C., Zhu, J.J., and Chen, Y.W. (2014b) Petrogenesis of late Cretaceous I-type granites in the southern Yidun terrane: new constraints on the Late Mesozoic tectonic evolution of the eastern Tibetan Plateau. Lithos, 208-209, 202-219.

Wang, X.S., Bi, X.W., Hu, R.Z., Leng, C.B., Yu, H.J., and Yin, G.H. (2015) S-Pb isotopic geochemistry of Xiuwacu magmatic hydrothermal Mo-W deposit in Zhongdian area, NW Yunnan: constrains on the sources of metal. Acta Petrologica Sinica, 31, 3171-3188.

Warner, S., Martin, R.F., Abdel-Rahman, A.-F.M., and Doig, R. (1998) Apatite as a monitor of fractionation, degassing, and metamorphism in the Sudbury igneous complex, Ontario. The Canadian Mineralogist, 36, 981-999.

Watson, E.B. and Green, T.H. (1981) Apatite/liquid partition coefficients for the rare earth elements and strontium. Earth and Planetary Science Letters, 56, 405-421

Webb, P.C., Tindle, A.G., and Ixer, R.A. (1992) W-Sn-Mo-Bi-Ag mineralization associated with Zinnwaldite-bearing granite from Glen Gairn, Scotland. Transactions of the institution of mining and metallurgy section b-applied earth science, 101, 59-72.

Webster, J.D. and Holloway, J.R. (1990) Partitioning of F and Cl between magmatic hydrothermal fluids and highly evolved granite magmas. Geological Society of America Special Paper, 246, 21-34.

DOI: https://doi.org/10.2138/am-2018-6224

White, J.C. (2003) Trace-element partitioning between alkali feldspar and peralkalic qurtz trachyte to rhyolite magma. Part□: Empirical equations for calculating trace-element partition coefficients of large-ion lithophile, high field-strength, and rare-earth elements. American Mineralogist, 88, 330-337.

White, J.C., Holt, G.S., Oarker, D.F., and Ren, M.H. (2003) Trace-element partitioning between alkali feldspar and peralkalic quartz trachyte to rhyolite magma. Part□: Systematics of trace-element partitioning. American Mineralogist, 88, 316-329.

Wolff, J.A. (1984) Variation in Nb/Ta during differentiation of phonolitic magma, Tenerife, Canary Islands. Geochimica et Cosmochimica Acta, 48, 1345-1348.

Wolff, J.A. and Storey, M. (1984) Zoning in highly alkaline magma bodies. Geological Magazine, 121, 563-575.

Wones, D.R. (1989) Significance of the assemblage titanite+magnetite+quartz in graniticrocks. American Mineralogist, 74, 744-749.

Xie, L., Wang, R.C., Chen, J., and Zhu, J.C. (2010) Mineralogical evidence for magmatic and hydrothermal processes in the Qitianling oxidized tin-bearing granite (Hunan, South China): EMP and (MC)-LA-ICPMS investigations of three types of titanite. Chemical Geology, 276, 53-68.

Xu, L.L., Bi, X.W., Hu, R.Z., Tang, Y.Y., Wang, X.S., and Xu, Y. (2015) LA-ICP-MS mineral chemistry of titanite and the geological implications for exploration of porphyry Cu deposits in the Jinshajiang-Red River alkaline igneous belt, SW China. Mineralogy and Petrology, 109, 181-200.

Yu, H.J. and Li, W.C. (2014) Geological characteristics of Tongchanggou superlarge molybdenum polymetallic deposit of Yidun arc in Sanjiang region, China. Acta Geologica Sinica-English Edition, 88, 639-640.

Yu, H.J., Li, W.C., Yin, G.H., Wang, J.H., Jiang, W.T., Wu, S., and Tang, Z. (2015) Geochronology, geochemistry and geological significance of the intrusion from the Tongchanggou Mo-Cu deposit, Northwestern Yunnan. Acta Petrologica Sinica, 31, 3217-3233.

Zhang, D. and Audėtat, A. (2016) What caused the formation of the giant Bingham Canyon porphyry Cu-Mo-Au Deposit? Insights from melt inclusions and magmatic sulfides. Economic Geology, 112, 221-244.

Zu, B., Xue, C.J., Zhao, X.B., Li, C., Zhao, Y., Yalikun, Y., Zhang, G.Z., and Zhao, Y. (2016) Geology, geochronology and geochemistry of granitic intrusions and the related ores at the Hongshan Cu-polymetallic deposit: Insights into the Late Cretaceous post-collisional porphyry-related mineralization systems in the southern Yidun arc, SW China. Ore Geology Reviews, 77, 25-42.

DOI: https://doi.org/10.2138/am-2018-6224

Figure Captions

Fig. 1. Regional geological map of the research area (modified from Wang et al., 2014a).

Fig. 2. Simplified geological maps for the CXWC and TXWC plutons (a), the TCG pluton (b) and the PL pluton (c) (modified from Wang et al., 2014b) .

Fig. 3. Total alkali *vs* SiO_2 diagram (Middlemost, 1994) (a) ; A/NK *vs* A/CNK diagram (Maniar and Piccoli, 1989) for the CXWC, TCG, PL and TXWC plutons in the southern Yidun Terrane (b).

Fig. 4. Chondrite-normalized REE diagrams and trace element diagrams for the selected plutons. Data are listed in Table 1. The chondrite values are from Sun and McDonough (1989).

Fig. 5. Plots of CaO *vs* ∑REE (a), CaO *vs* TiO_2 (b), TiO_2 *vs* (Fe_2O_3+Al_2O_3) (c), F *vs* (Fe_2O_3+Al_2O_3) (d), TiO_2 *vs* (Nb+Ta) (e), and TiO_2 *vs* F (f) of titanite from the selected plutons.

Fig. 6. The geochemical behavior of Sr, U, Th, Y, REE, Nb, and Ta between titanite and whole rock. The average contents of whole-rocks were used to represent the magmatic composition, avoiding the possible effect from the cumulate of minerals.

Fig. 7. Chondrite-normalized REE patterns for titanite crystals from the selected plutons. Data are listed in Table 2. The chondrite values are from Sun and McDonough (1989).

Fig. 8. The modes of occurrence of titanite in the rock samples from the selected plutons. *Ab*, albite; *Ap*, apatite; *Bt*, biotite; *Chl*, chlorite; *Hbl*, hornblend; *Pl*, plagioclase; *Qtz*, quartz; *Ttn*, titanite.

Fig. 9. Plots of $(La/Yb)_N$ and $(Sm/Yb)_N$ *vs* Sr contents for titanite crystals from the selected plutons.

Fig. 10. Plots of δEu *vs* δCe (a), Ga *vs* δCe (b) and Ga *vs* (Fe_2O_3/Al_2O_3) (c) for titanite crystals from the selected plutons.

Fig. 11. Plots of log(fO_2) *vs* titanite Ga contents (a) and Fe_2O_3/Al_2O_3 (b). The values of log(fO_2) were calculated from zircon data listed in Table.4.

Fig. 12. Plots of log(fO_2) *vs* 1000/T. The oxygen fugacity of samples was calculated from zircon Ce anomalies using the method of Trail et al. (2012). The temperatures of samples were calculated using the Ti-in-zircon thermometry of Ferry and Watson (2007). The zircon compositions are listed in Table 4. Buffers: HM, Fe_2O_3-Fe_3O_4; NNO, Ni-NiO; QFM, SiO_2-Fe_2SiO_4-Fe_3O_4; MW, Fe_3O_4-FeO. The shaded fields show MoS_2-saturated melt inclusions from Audėtat et al. (2011). The dashed lines show the thermodynamically predicted

DOI: https://doi.org/10.2138/am-2018-6224

MoS_2 solubilities in the magmas with fS_2 fixed at the value corresponding to the pyrrhotite-magnetite-fayalite assemblage (Audėtat et al., 2011).

Fig. 13. Classification of the CWXC, TCG PL and TXWC plutons using the tectonic discrimination diagram of Pearce et al. (1984). The shaded fields show MoS_2-saturated and -undersaturated felsic melt inclusions from around the world (Audėtat et al., 2011).

Fig. 14. Plots of TiO_2 *vs* Mo (a) and Sr *vs* Mo (b) for titanite crystals from the selected plutons.

Fig. 15. Variations of Fe_2O_3/Al_2O_3 and Mo-F in titanite from Mo-mineralized and non-mineralized granitic plutons.

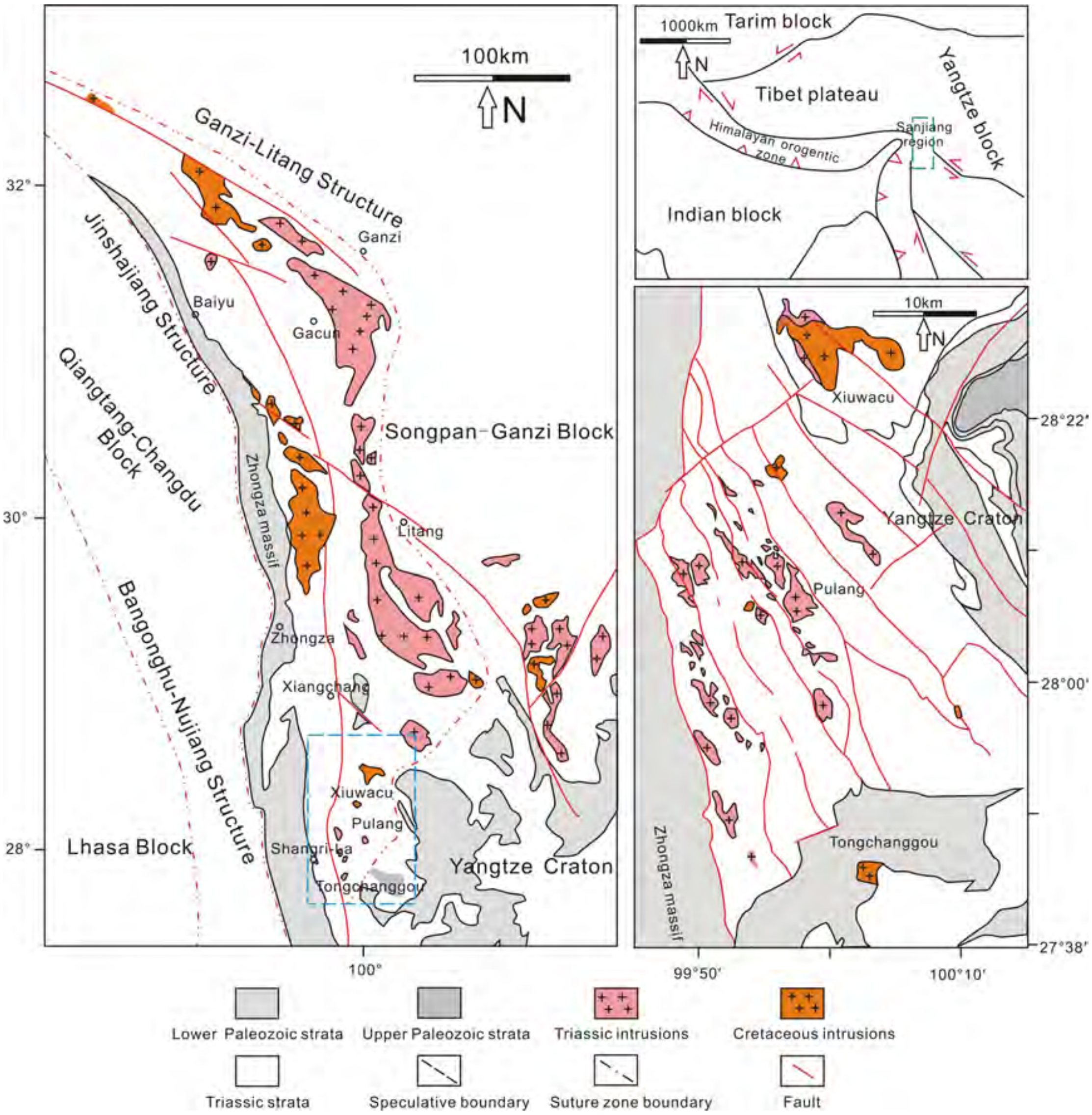
100km
N
Ganzi-Litang Structure
Ganzi
Baiyu
Gacun
Jinshajiang Structure
Qiangtang-Changdu Block
Songpan-Ganzi Block
Zhongza massif
Litang
Zhongza
Xiangcheng
Bangonghu-Nujiang Structure
Xiuwacu
Pulang
Shangri-La
Tongchanggou
Lhasa Block
Yangtze Craton
32°
30°
28°
100°
1000km
Tarim block
Tibet plateau
Yangtze block
Himalayan orogentic zone
Sanjiang region
Indian block
10km
Xiuwacu
Yangtze Craton
Pulang
Tongchanggou
Zhongza massif
28°22′
28°00′
27°38′
99°50′
100°10′
Lower Paleozoic strata
Upper Paleozoic strata
Triassic intrusions
Cretaceous intrusions
Triassic strata
Speculative boundary
Suture zone boundary
Fault

Fig. 1

This is a preprint, the final version is subject to change, of the American Mineralogist (MSA)
Cite as Authors (Year) Title. American Mineralogist, in press.
DOI: https://doi.org/10.2138/am-2018-6224

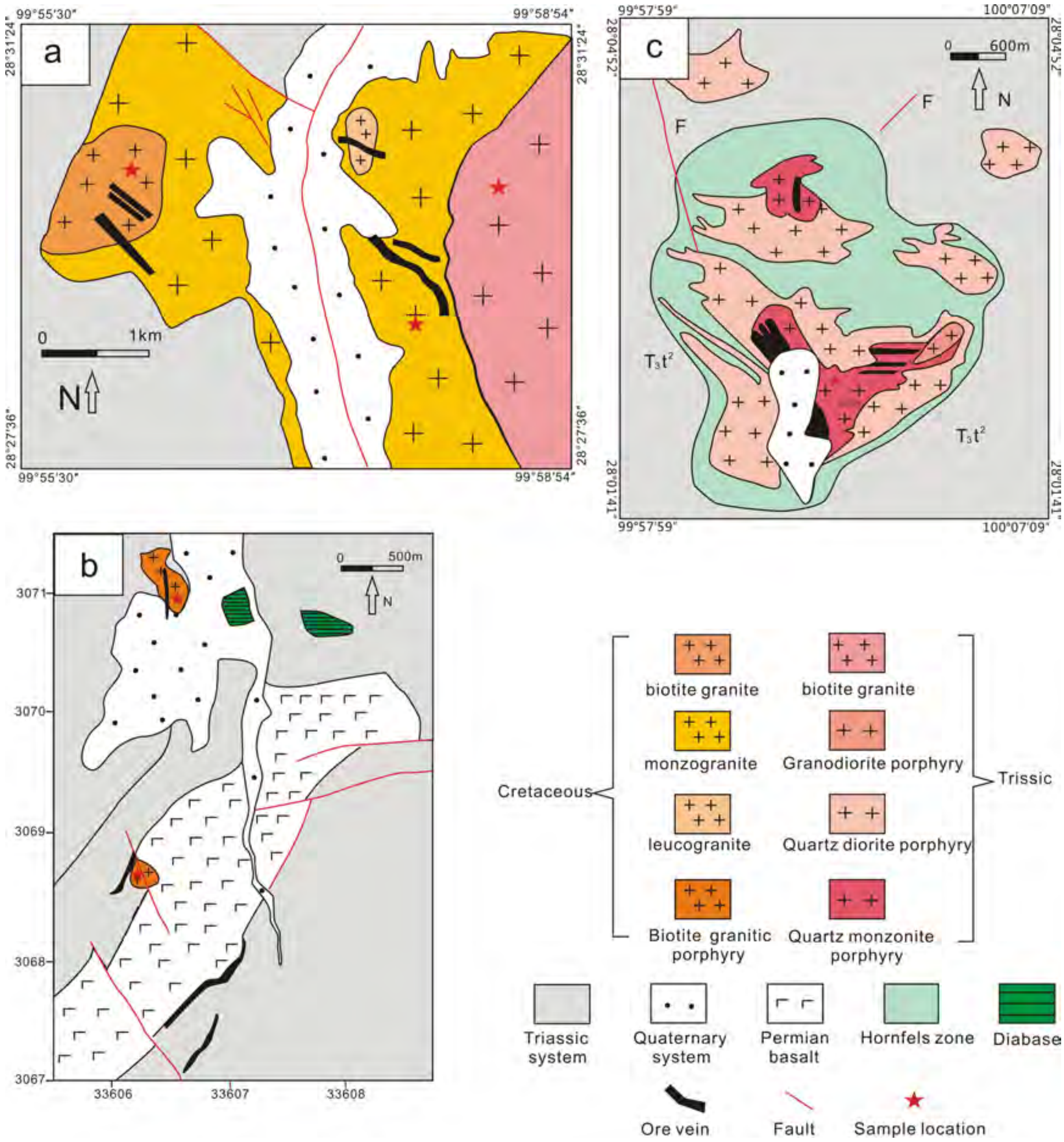

Fig.2

This is a preprint, the final version is subject to change, of the American Mineralogist (MSA)
Cite as Authors (Year) Title. American Mineralogist, in press.
DOI: https://doi.org/10.2138/am-2018-6224

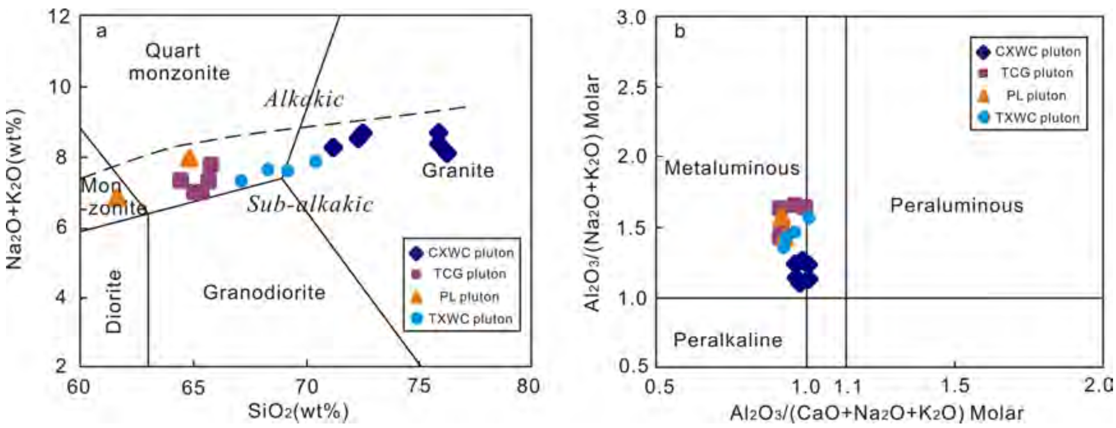

Fig.3

This is a preprint, the final version is subject to change, of the American Mineralogist (MSA)
Cite as Authors (Year) Title. American Mineralogist, in press.
DOI: https://doi.org/10.2138/am-2018-6224

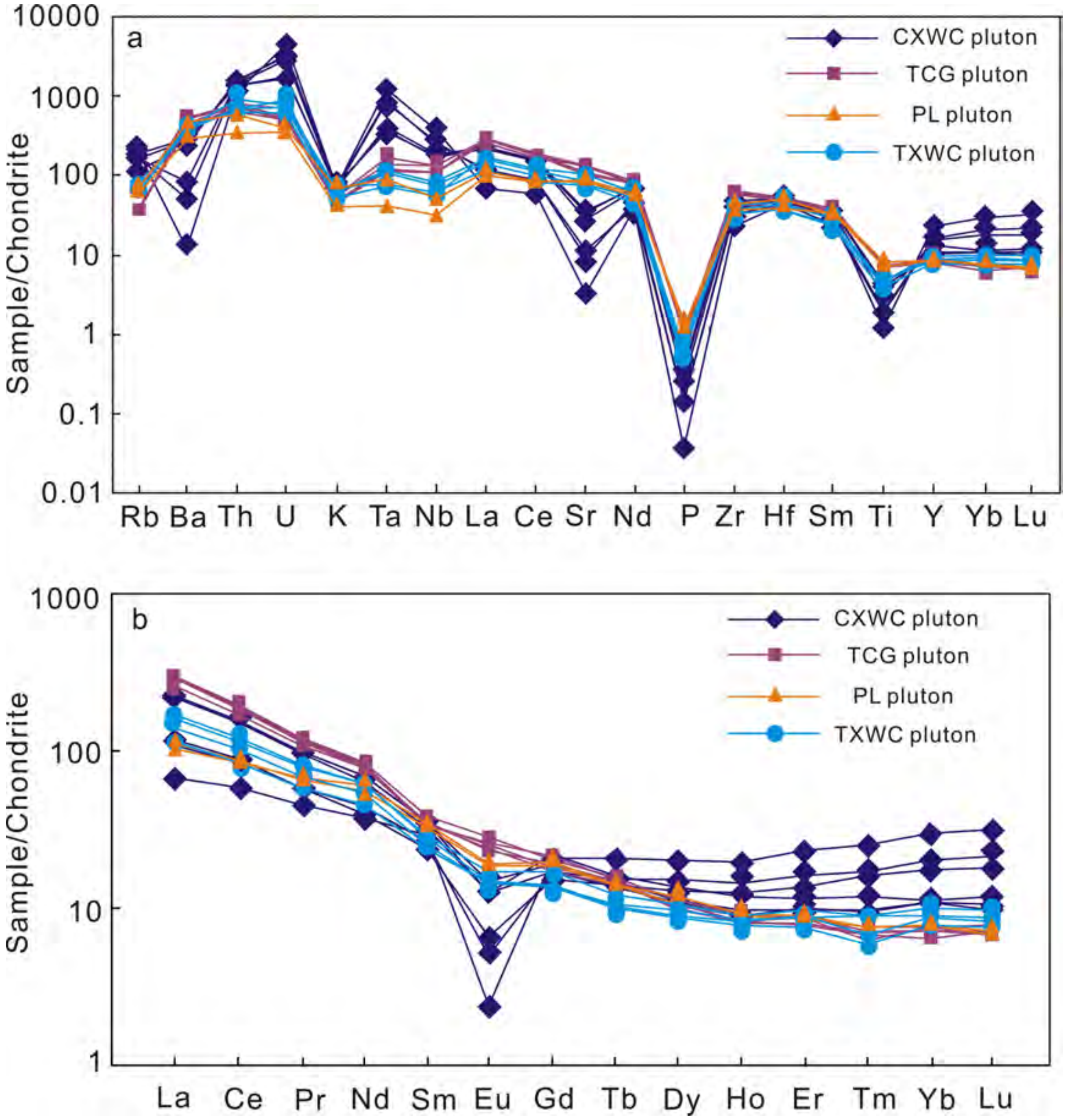

Fig.4

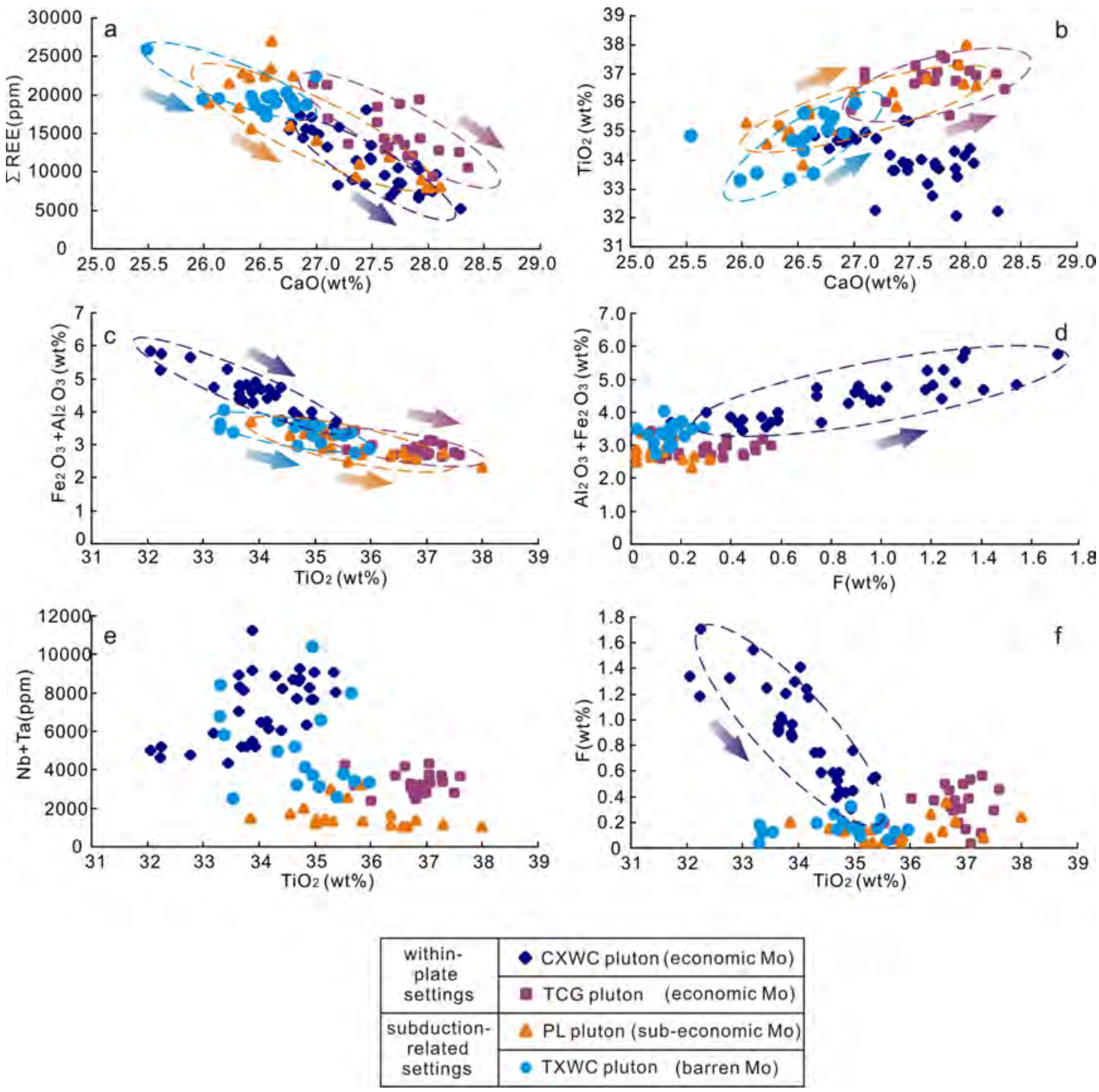
a
ΣREE(ppm)
CaO(wt%)
b
TiO2 (wt%)
CaO(wt%)
c
Fe2O3 +Al2O3 (wt%)
TiO2 (wt%)
d
Al2O3 +Fe2O3 (wt%)
F(wt%)
e
Nb+Ta(ppm)
TiO2 (wt%)
f
F(wt%)
TiO2 (wt%)
within-plate settings
CXWC pluton (economic Mo)
TCG pluton (economic Mo)
subduction-related settings
PL pluton (sub-economic Mo)
TXWC pluton (barren Mo)

Fig.5

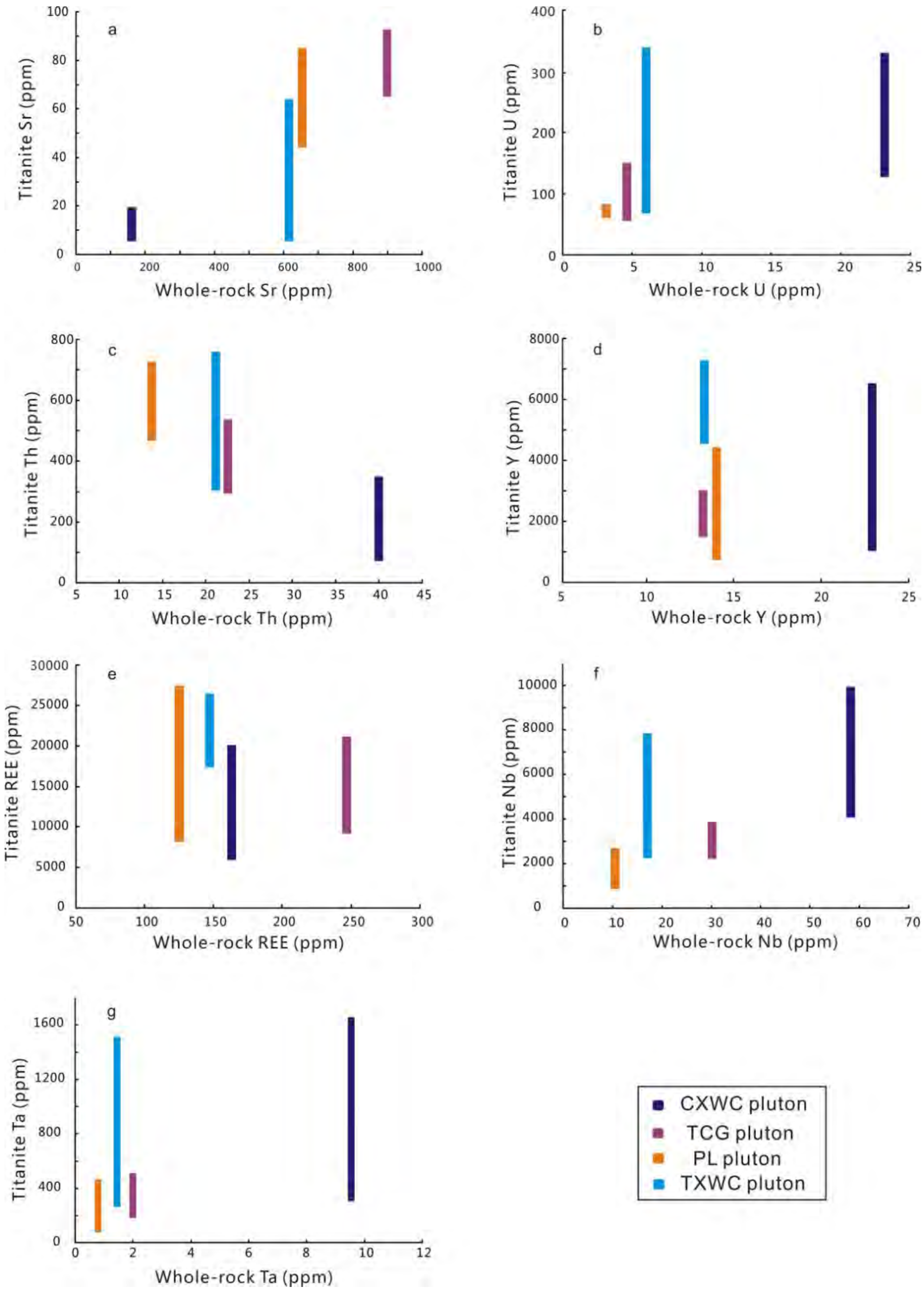
a
Titanite Sr (ppm)
Whole-rock Sr (ppm)
b
Titanite U (ppm)
Whole-rock U (ppm)
c
Titanite Th (ppm)
Whole-rock Th (ppm)
d
Titanite Y (ppm)
Whole-rock Y (ppm)
e
Titanite REE (ppm)
Whole-rock REE (ppm)
f
Titanite Nb (ppm)
Whole-rock Nb (ppm)
g
Titanite Ta (ppm)
Whole-rock Ta (ppm)
CXWC pluton
TCG pluton
PL pluton
TXWC pluton

Fig.6

This is a preprint, the final version is subject to change, of the American Mineralogist (MSA)
Cite as Authors (Year) Title. American Mineralogist, in press.
DOI: https://doi.org/10.2138/am-2018-6224

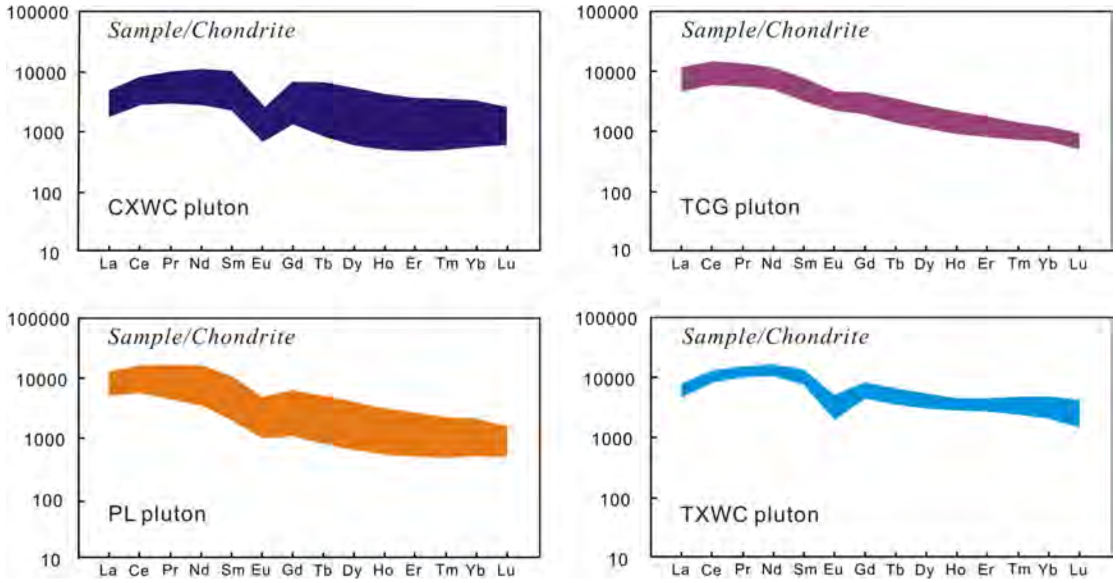

Fig.7

This is a preprint, the final version is subject to change, of the American Mineralogist (MSA)
Cite as Authors (Year) Title. American Mineralogist, in press.
DOI: https://doi.org/10.2138/am-2018-6224

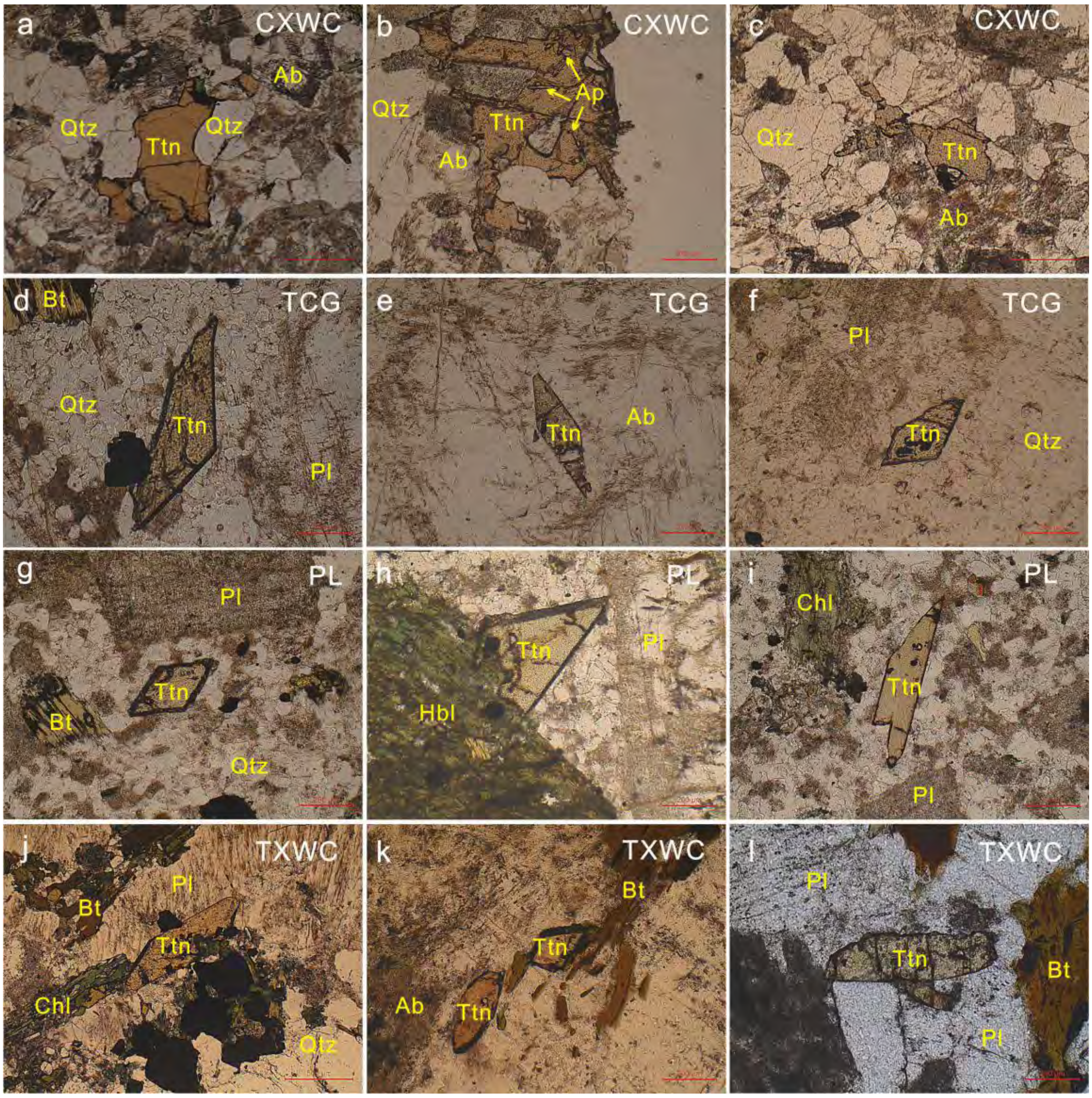

Fig.8

DOI: https://doi.org/10.2138/am-2018-6224

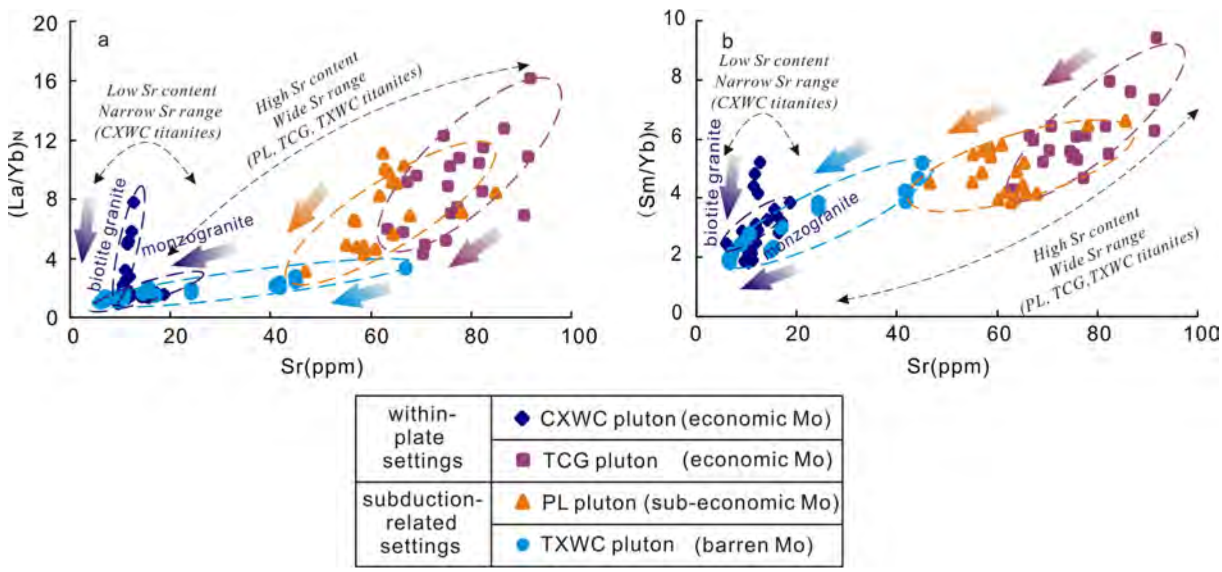

Fig.9

This is a preprint, the final version is subject to change, of the American Mineralogist (MSA)
Cite as Authors (Year) Title. American Mineralogist, in press.
DOI: https://doi.org/10.2138/am-2018-6224

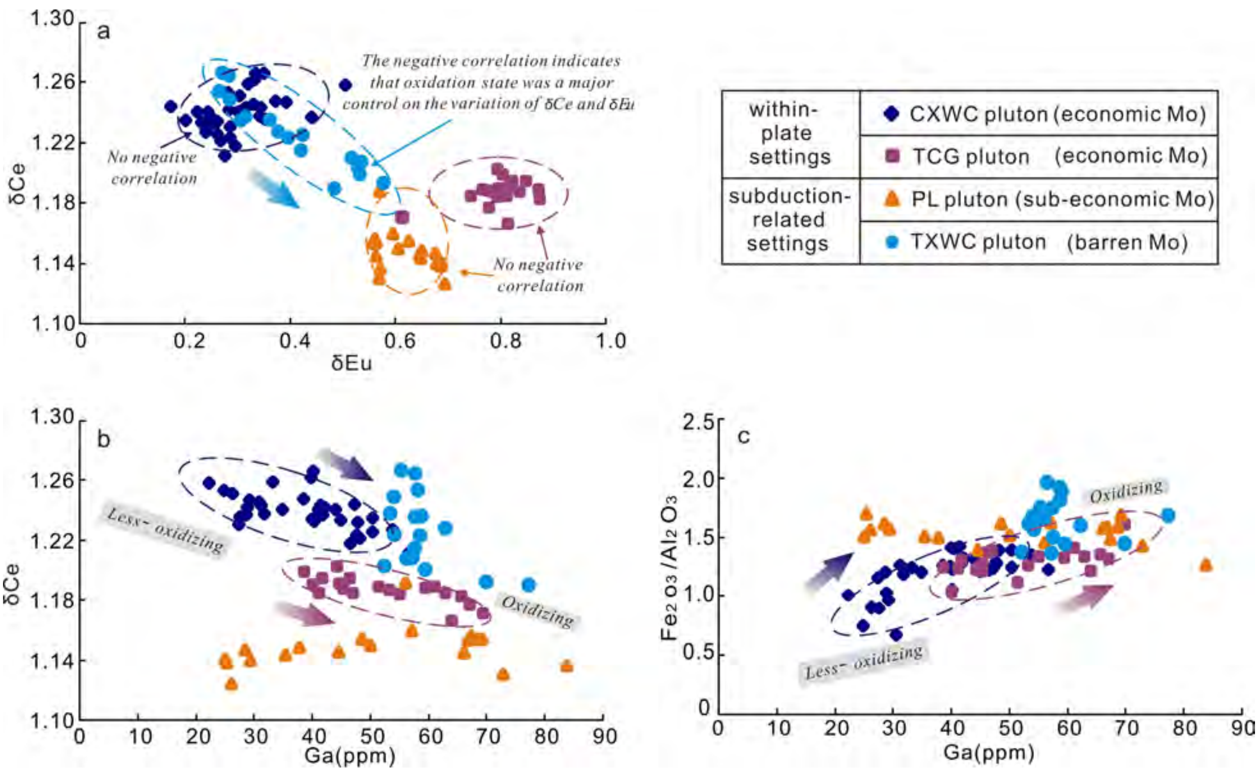

Fig.10

DOI: https://doi.org/10.2138/am-2018-6224

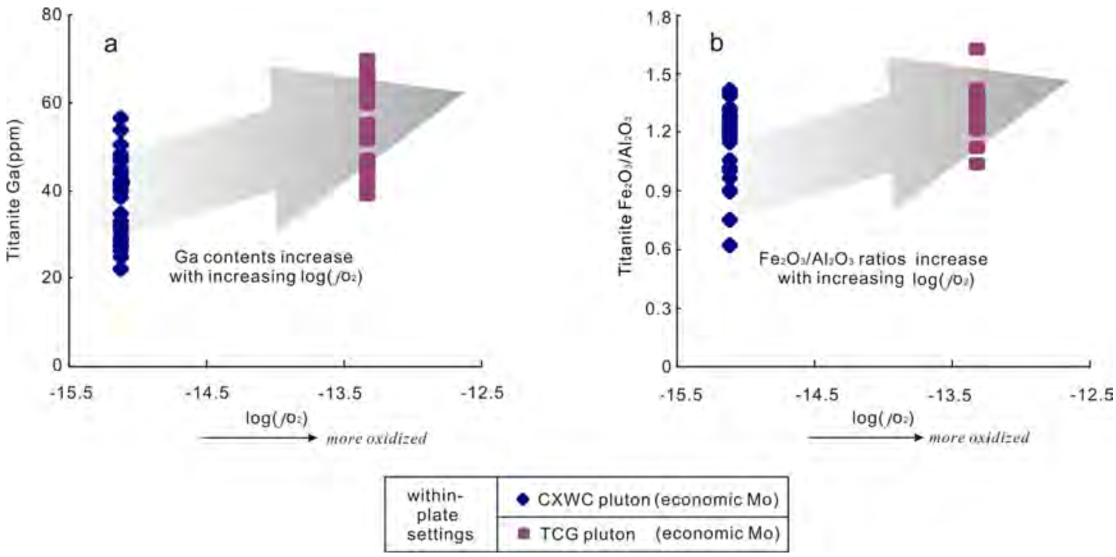

Fig.11

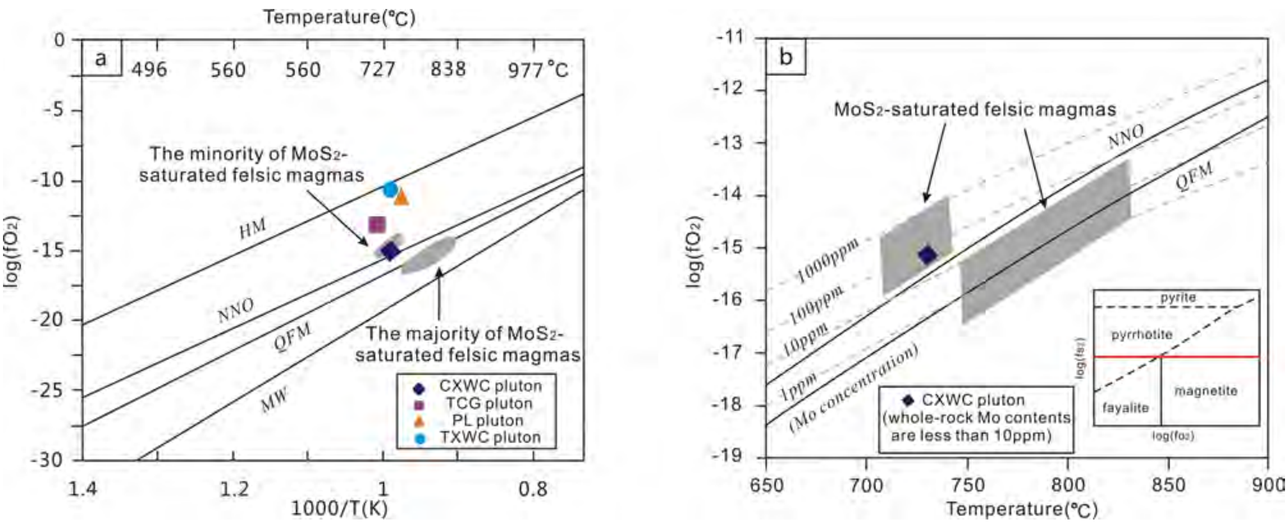
Temperature(°C)
a
496
560
560
727
838
977°C
The minority of MoS2-saturated felsic magmas
HM
NNO
QFM
MW
The majority of MoS2-saturated felsic magmas
CXWC pluton
TCG pluton
PL pluton
TXWC pluton
log(fO2)
1000/T(K)
b
MoS2-saturated felsic magmas
NNO
QFM
1000ppm
100ppm
10ppm
1ppm
(Mo concentration)
CXWC pluton (whole-rock Mo contents are less than 10ppm)
pyrite
pyrrhotite
magnetite
fayalite
log(fS2)
log(fO2)
Temperature(°C)

Fig.12

This is a preprint, the final version is subject to change, of the American Mineralogist (MSA)
Cite as Authors (Year) Title. American Mineralogist, in press.
DOI: https://doi.org/10.2138/am-2018-6224

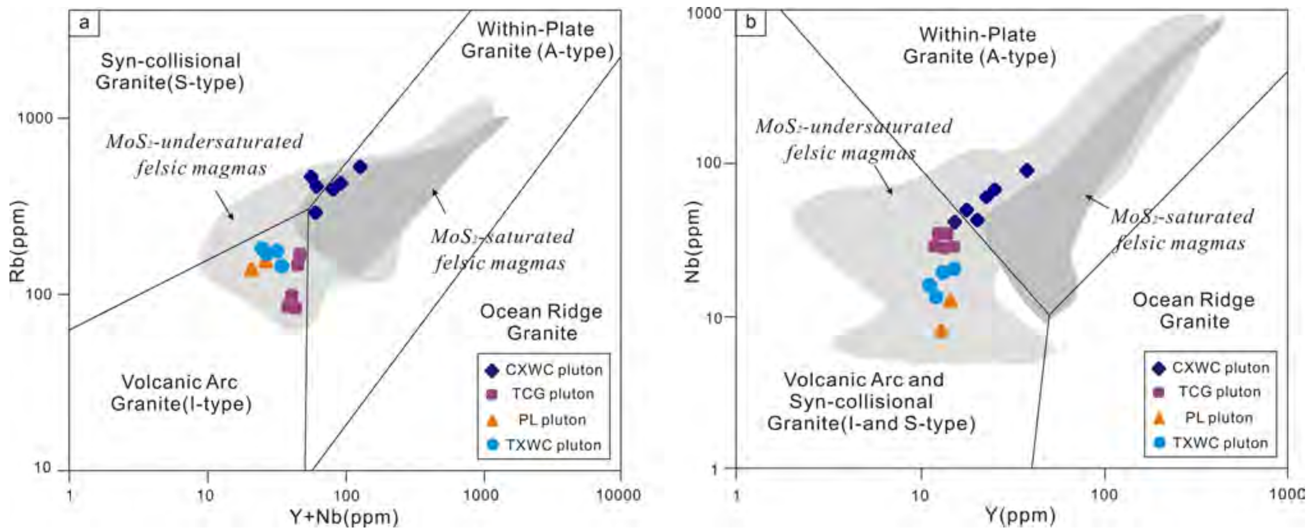

Fig.13

DOI: https://doi.org/10.2138/am-2018-6224

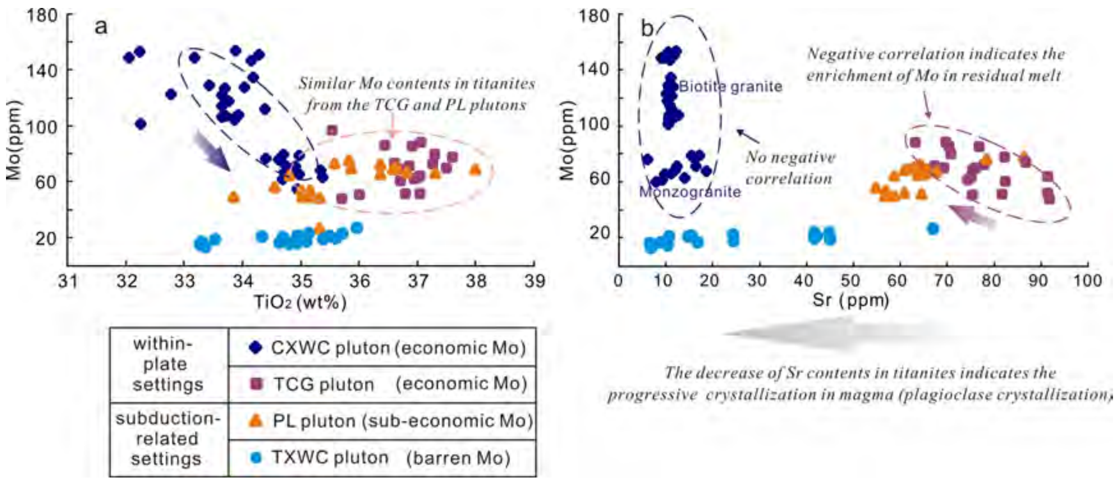

Fig.14

DOI: https://doi.org/10.2138/am-2018-6224

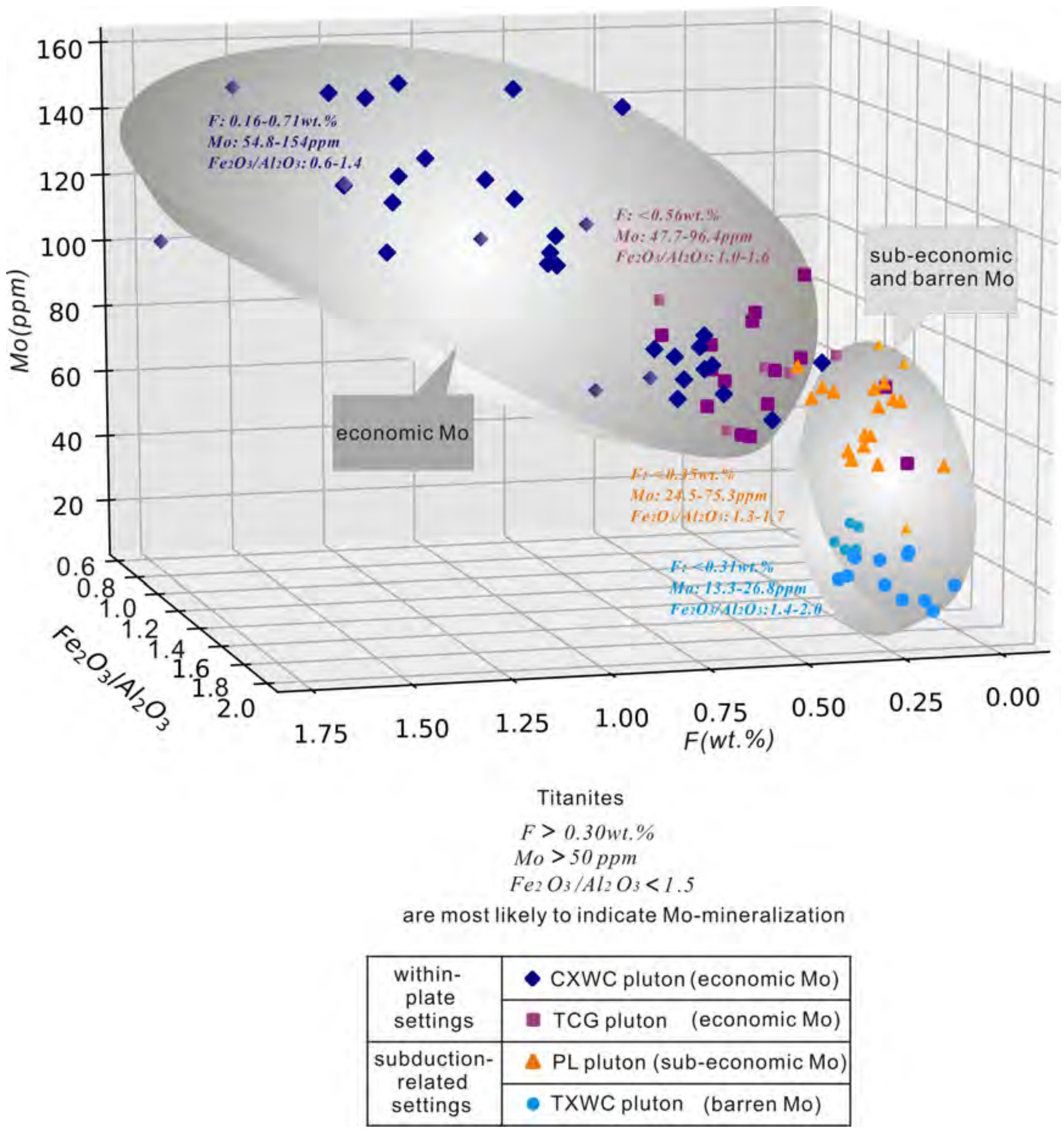

Fig.15

This is a preprint, the final version is subject to change, of the American Mineralogist (MSA)
Cite as Authors (Year) Title. American Mineralogist, in press.
DOI: https://doi.org/10.2138/am-2018-6224

Table.1 The results of major (wt.%) and trace elements (ppm) analyzes for selected four plutons from southern Yidun Arc

Pluton	Xiuwacu Cretaceous pluton						Tongchanggou pluton					Pulang pluton		Xiuwacu Trissic pluton			
Petrology	Biotite granite			Monzogranite			Biotite granite porphyry					Quartz monzonitic porphyry		Biotite granite			
SiO_2	71.19	72.41	72.47	75.83	75.75	76.19	64.63	65.32	65.68	65.72	65.84	65.04	61.68	70.34	68.34	66.93	69.24
Al_2O_3	13.60	13.86	13.53	12.48	12.40	12.23	14.23	15.78	15.76	14.93	16.01	14.39	14.84	13.96	14.86	15.46	14.31
Fe_2O_{3T}	2.39	2.24	1.87	1.54	1.85	1.78	3.49	4.06	4.02	3.55	3.91	4.28	3.90	2.72	3.23	3.65	2.95
MgO	0.55	0.50	0.34	0.20	0.10	0.20	1.34	1.36	1.40	1.16	1.27	2.43	3.97	1.02	1.23	1.71	1.20
CaO	1.45	1.47	1.34	0.81	0.63	0.80	2.85	3.45	3.42	2.85	3.77	2.71	3.46	2.41	2.85	3.00	2.67
Na_2O	3.82	3.86	3.45	3.62	3.89	3.60	3.56	4.00	3.95	4.06	4.06	3.21	4.00	3.23	3.62	3.81	3.54
K_2O	4.42	4.62	5.03	4.81	4.61	4.54	3.66	2.96	3.02	3.59	3.19	4.58	2.70	4.69	3.95	3.37	4.07
P_2O_5	0.11	0.09	0.07	0.04	0.01	0.04	0.27	0.26	0.28	0.28	0.30	0.39	0.32	0.14	0.16	0.19	0.16
TiO_2	0.33	0.29	0.23	0.14	0.09	0.15	0.52	0.55	0.56	0.53	0.53	0.54	0.61	0.28	0.33	0.35	0.33

DOI: https://doi.org/10.2138/am-2018-6224

MnO	0.06	0.06	0.04	0.04	0.03	0.04	0.06	0.06	0.06	0.04	0.06	0.02	0.02	0.05	0.07	0.05	0.06
L.O.I.	1.06	0.82	0.56	0.34	0.45	0.31	4.90	1.65	1.73	3.13	0.65	1.97	3.38	0.89	0.95	1.11	1.09
Total	99.07	100.34	99.00	99.88	99.84	99.92	99.72	99.68	100.11	100.09	99.85	99.77	99.04	99.90	99.79	99.84	99.79
Na_2O+K_2O	8.24	8.48	8.48	8.43	8.50	8.14	7.22	6.96	6.97	7.65	7.25	7.79	6.70	7.92	7.57	7.18	7.61
K_2O/Na_2O	1.16	1.20	1.46	1.33	1.19	1.26	1.03	0.74	0.76	0.88	0.79	1.43	0.68	1.45	1.09	0.88	1.15
A/CNK	0.99	0.99	1.00	0.99	0.99	0.99	0.95	0.98	0.98	0.95	0.94	0.95	0.94	0.94	0.96	1.00	0.95
Rittmann index	2.41	2.45	2.44	2.16	2.21	2.00	2.41	2.17	2.14	2.58	2.30	2.75	2.40	2.29	2.26	2.15	2.21
Ga	20.0	21.5	18.2	18.2	23.1	20.7	18.9	19.9	19.5	18.9	19.1	17.3	20.4	15.2	16.4	18.9	18.1
Rb	376	436	260	381	500	413	159	83	90	148	83	164	141	166	144	169	177
Ba	672	700	586	196	29	124	1130	1025	1005	1345	1270	1165	714	951	928	1050	887
Sr	255	249	205	82	24	69	754	951	979	810	983	615	653	536	624	757	560
Zr	175	183	164	123	88	141	171	228	241	239	252	175	149	125	145	164	128
Nb	46.42	40.60	42.43	61.95	92.20	65.00	33.38	27.80	27.30	33.40	27.50	12.80	7.90	15.10	20.30	13.50	18.60

Mo	1.76	2.76	2.79	5.23	1.13	2.83	1.1	1.15	1.22	2.64	5.14	1.44	0.76	1.06	4.29	0.74	1.62
Hf	4.96	5.50	4.91	4.54	4.70	6.00	4.37	5.10	5.60	5.60	5.70	5.40	4.20	3.90	4.60	4.80	3.90
Ta	5.80	5.30	5.02	12.27	17.40	11.70	2.42	1.60	1.70	2.00	1.70	1.30	0.60	1.10	1.60	1.00	1.50
Th	40.10	39.20	44.70	43.70	32.60	41.40	22.80	21.30	19.05	23.60	22.30	17.40	10.10	26.60	19.95	18.05	20.30
U	14.00	13.15	25.00	26.40	35.40	23.50	4.50	4.20	4.05	5.68	4.01	3.26	2.88	6.12	5.79	4.93	6.99
La	53.80	52.30	51.50	28.00	16.20	26.10	68.20	70.30	62.20	69.90	70.70	26.80	24.10	27.00	38.40	40.90	33.50
Ce	95.6	93.4	92.0	54.6	35.9	52.3	113.0	113.0	105.0	117.0	118.5	53.2	52.0	51.3	71.1	75.0	62.1
Pr	9.53	9.39	9.12	5.57	4.35	5.53	11.20	10.85	10.40	11.25	11.55	6.25	6.33	5.52	7.58	7.76	6.66
Nd	32.1	32.7	29.8	18.3	17.5	20.9	36.9	36.7	35.8	37.9	39.5	26.2	28.1	21.4	28.9	28.9	25.4
Sm	5.36	5.40	4.95	3.69	4.51	4.10	5.17	5.26	5.45	5.24	5.96	4.96	5.25	3.61	4.49	4.36	3.84
Eu	0.87	0.72	0.73	0.38	0.14	0.29	1.50	1.39	1.36	1.46	1.64	1.07	1.10	0.83	0.99	0.87	0.84
Gd	3.94	3.50	4.52	3.11	4.29	3.55	4.41	3.55	3.89	3.68	4.13	3.85	4.02	2.81	3.46	2.85	2.82
Tb	0.56	0.51	0.60	0.52	0.78	0.57	0.58	0.52	0.55	0.55	0.58	0.52	0.53	0.37	0.45	0.39	0.40
Dy	2.85	2.79	3.49	3.29	5.12	3.91	2.53	2.70	2.60	2.47	2.83	2.68	3.00	2.20	2.72	2.27	2.44

DOI: https://doi.org/10.2138/am-2018-6224

Ho	0.55	0.51	0.66	0.71	1.11	0.82	0.45	0.47	0.50	0.47	0.52	0.51	0.52	0.44	0.51	0.47	0.48
Er	1.60	1.67	1.88	2.26	3.85	2.69	1.34	1.45	1.44	1.28	1.45	1.40	1.47	1.25	1.63	1.46	1.43
Tm	0.25	0.24	0.30	0.41	0.65	0.44	0.18	0.18	0.16	0.17	0.19	0.19	0.19	0.15	0.23	0.17	0.23
Yb	1.86	1.85	1.90	2.99	5.09	3.42	1.22	1.22	1.29	1.09	1.28	1.32	1.31	1.32	1.68	1.47	1.54
Lu	0.27	0.25	0.30	0.46	0.81	0.54	0.17	0.18	0.17	0.18	0.20	0.18	0.17	0.19	0.25	0.21	0.22
Y	17.3	15.9	20.2	23.5	36.3	25.2	13.6	12.7	13.2	12.8	15.1	13.7	13.8	11.7	14.7	12.6	13.7
∑REE	209	205	202	124	100	125	247	248	231	253	259	129	128	118	162	167	142
$(La/Yb)_N$	20.75	20.28	19.44	6.72	2.28	5.47	40.10	41.33	34.59	46.00	39.62	14.56	13.20	14.67	16.40	19.96	15.60
$(La/Sm)_N$	6.48	6.25	6.72	4.90	2.32	4.11	8.52	8.63	7.37	8.61	7.66	3.49	2.96	4.83	5.52	6.06	5.63
$(Sm/Yb)_N$	3.20	3.24	2.89	1.37	0.98	1.33	4.71	4.79	4.69	5.34	5.17	4.18	4.45	3.04	2.97	3.30	2.77
δEu	0.58	0.51	0.47	0.34	0.10	0.23	0.96	0.98	0.90	1.02	1.01	0.75	0.73	0.80	0.77	0.75	0.78
δCe	1.04	1.03	1.04	1.07	1.05	1.07	1.00	1.00	1.01	1.02	1.02	1.01	1.03	1.03	1.02	1.03	1.02

Rittmann index= $(Na_2O + K_2O)^2/(SiO_2 - 43)$, $\delta Eu=Eu_N/(Sm_N{*}Gd_N)^{1/2}$, $\delta Ce=Ce_N/(La_N{*}Pr_N)^{1/2}$,

This is a preprint, the final version is subject to change, of the American Mineralogist (MSA)
Cite as Authors (Year) Title. American Mineralogist, in press.
DOI: https://doi.org/10.2138/am-2018-6224

Table.2 The results of major (wt.%) and trace elements (ppm) analyzes for titanites from selected four plutons by EPMA and LA-ICP-MS

DOI: https://doi.org/10.2138/am-2018-6224

Intrusion	CXWC pluton																					Stdev
Petrology	Biotite granite																					n=21
CaO	27.76	27.36	27.49	27.35	27.99	27.61	27.32	27.9	27.7	27.44	27.48	27.92	27.19	27.92	27.67	27.74	28.29	27.73	28.07	28.04	27.91	0.29
TiO_2	33.7	33.64	33.88	33.65	34.15	34.03	34.18	34.29	32.77	33.94	33.65	32.06	32.25	33.44	33.19	33.78	32.24	33.89	33.88	34.4	33.72	0.68
Na_2O	0.02	bdl	0.03	0.05	0.03	0.04	bdl	0.04	0.02	0.04	0.03	0.03	0.04	0.02	0.03	bdl	0.03	0.02	0.04	bdl	0.03	0.01
F	1.02	0.91	0.9	0.96	1.24	1.41	1.18	0.74	1.32	1.3	0.93	1.34	1.71	1.25	1.55	1.21	1.19	0.96	0.87	0.74	0.99	0.26
MgO	0.05	0.05	0.05	0.04	0.05	0.03	0.05	0.05	0.07	0.05	0.03	0.12	0.11	0.05	0.06	0.04	0.1	0.05	0.06	0.05	0.05	0.02
Al_2O_3	2.19	1.99	1.93	1.95	2.33	2.07	2.13	1.86	2.87	2.17	1.88	3.07	3.56	2.41	2.72	2.39	2.63	1.93	1.9	2.2	2.12	0.45
Fe_2O_3	2.59	2.8	2.69	2.42	2.09	2.62	2.55	2.63	2.77	2.73	2.66	2.76	2.19	2.89	2.03	2.44	2.64	2.38	2.36	2.53	2.24	0.24
MnO	0.18	0.21	0.23	0.21	0.14	0.17	0.18	0.17	0.2	0.18	0.19	0.18	0.32	0.21	0.19	0.19	0.14	0.21	0.21	0.19	0.27	0.04
P_2O_5	0.03	0.01	0.05	0.03	0.04	0.01	0.05	0.04	0.04	0.03	0.05	0.03	0.01	0.02	0.03	0.05	0.03	0.04	0.01	0.01	0.05	0.01
SiO_2	31.39	30.74	30.71	30.68	31.24	31.11	30.93	30.89	31.02	31.54	31.09	31.23	30.83	31.08	31.42	30.99	31.07	30.75	31.2	30.91	30.85	0.24
F=O	0.43	0.38	0.38	0.4	0.52	0.59	0.5	0.31	0.56	0.55	0.39	0.56	0.72	0.53	0.65	0.51	0.5	0.4	0.37	0.31	0.42	0.11

Total	98.26	97.09	97.32	96.72	98.58	98.26	97.85	98.07	97.98	98.62	97.36	97.92	97.29	98.5	98.04	98.11	97.61	97.34	98.02	98.53	97.6	0.53
Fe_2O_3/Al_2O_3	1.19	1.41	1.39	1.24	0.89	1.26	1.2	1.42	0.97	1.26	1.41	0.9	0.62	1.2	0.75	1.02	1.01	1.23	1.25	1.15	1.06	0.22
$Fe_2O_3+Al_2O_3$	4.78	4.79	4.61	4.37	4.42	4.69	4.69	4.49	5.64	4.9	4.54	5.83	5.75	5.3	4.75	4.83	5.26	4.31	4.26	4.73	4.35	0.47
Cu	0.4	0.72	0.82	0.71	0.68	0.62	0.49	0.66	0.7	0.79	0.76	0.69	0.79	0.7	0.79	0.72	0.71	0.68	0.65	0.75	0.74	0.10
Mo	127	114	105	122	147	128	134	151	123	108	106	149	101	129	149	118	153	154	106	112	107	18.30
Ga	31.85	39.9	40.26	33.16	27.62	38.56	34.88	41.44	29.28	31.31	41.07	26.29	30.8	28.67	24.82	28.81	22.21	40.15	39.73	27.31	40.21	6.19
Ge	39.38	48.46	49.91	40.09	37.66	46.73	39.74	52.76	37.68	40.00.	49.27	43.71	38.12	40.36	41.46	37.6	35.84	48.4	47.83	34.16	47.7	5.53
Sr	10.67	10.87	10.69	11.18	10.92	11.39	11.04	11.8	10.36	10.78	10.63	9.73	10.52	10.6	9.62	10.4	10.46	12.16	11.61	11.29	12.63	0.73
Y	2511	3868	4165	2195	2461	1234	1817	2301	2431	2575	4166	2739	2639	1993	2931	3522	1735	1247	1234	2755	966	931
Zr	351	438	449	445	308	491	443	526	323	349	410	294	337	343	249	304	267	835	453	299	1327	240
Nb	4617	7341	7498	6201	5938	5854	5195	8158	4316	4617	6882	4719	4661	4006	4905	4664	4362	10264	4934	5360	7169	1583
La	756	838	823	873	634	922	880	940	628	711	811	426	691	653	413	612	403	1129	907	610	1126	205
Ce	2995	3657	3605	3465	2574	3855	3476	3994	2587	2884	3645	1928	2804	2557	1911	2584	1731	4467	3895	2415	4446	812
Pr	466	630	625	522	411	623	537	660	412	455	640	335	441	393	338	425	282	663	632	380	658	126

DOI: https://doi.org/10.2138/am-2018-6224

Nd	2099	3028	3036	2271	1874	2732	2322	3019	1887	2056	3139	1648	2006	1756	1706	2028	1316	2768	2816	1738	2746	554
Sm	513	806	818	512	492	519	493	671	487	526	863	474	515	422	526	603	348	513	553	496	489	130
Eu	53.82	63.25	62.01	48.27	54.1	48.89	42.53	58.63	58.25	55.43	63.09	45.99	52.83	55.38	47.87	60.39	54.57	44.22	46.84	45.27	42.59	6.79
Gd	449	677	706	414	447	312	374	481	424	462	730	450	466	350	511	589	313	319	337	470	284	129
Tb	71.22	106.02	111.24	63.85	72.48	38.17	55.1	66.96	69.05	75.15	115.85	75.67	75.98	53.88	86.88	100.73	49.99	41.41	41.12	79.92	33.72	23.91
Dy	429	628	668	375	434	196	320	366	406	446	678	458	454	313	525	615	297	218	208	484	166	153
Ho	83.64	123.29	131.81	73.03	83.22	36.99	61.53	71.61	80.52	87.53	135.21	90.84	89.77	62.35	101.46	119.84	57.51	41.17	38.53	93.64	30.41	30.77
Er	235	355	380	205	232	104	170	205	225	245	386	256	250	176	277	335	158	116	106	262	84	88.42
Tm	37.38	56.86	61.55	32.39	36.47	17.07	27.09	33.3	36.28	39.31	63.18	40.94	40.03	28.42	44.37	53.57	25.01	18.46	16.94	41.81	13.54	14.32
Yb	276	417	454	243	267	133	199	246	265	286	464	301	292	213	327	389	181	140	126	306	103	104
Lu	41.03	59.13	64.91	35.87	38.22	21.9	30.13	37.33	38.88	41.62	67.11	44.36	42.44	32.34	48.28	55.81	28.28	21.85	19.83	43.49	17.09	14.12
Hf	31	55.05	63.55	40.63	28.4	46.95	44.62	49.88	29.25	31.51	42.17	25.6	31.98	28.22	29.14	28.78	23.19	60.44	47.62	26.31	131.88	23.72
Ta	591	1588	1646	861	572	606	962	720	463	567	1449	305	556	350	1005	546	288	997	554	686	950	393
Th	112	122	120	125	97	142	124	188	99	108	123	87	103	97	70	101	79	225	134	83	197	39.56

DOI: https://doi.org/10.2138/am-2018-6224

U	201	203	199	208	166	239	217	275	180	192	205	143	185	174	119	178	133	328	229	149	302	52.46
∑REE	8506	11444	11546	9131	7650	9559	8988	10850	7604	8371	11800	6574	8221	7066	6863	8570	5244	10499	9743	7464	10241	1786
$(La/Sm)_N$	0.95	0.67	0.65	1.1	0.83	1.15	1.15	0.9	0.83	0.87	0.61	0.58	0.87	1	0.51	0.66	0.75	1.42	1.06	0.79	1.49	0.26
$(La/Yb)_N$	1.97	1.44	1.3	2.58	1.71	4.96	3.17	2.74	1.7	1.79	1.25	1.02	1.69	2.2	0.91	1.13	1.59	5.8	5.16	1.43	7.83	1.85
$(Sm/Yb)_N$	2.07	2.15	2	2.34	2.05	4.33	2.75	3.03	2.04	2.05	2.07	1.75	1.96	2.2	1.79	1.72	2.13	4.08	4.88	1.81	5.27	1.08
δEu	0.34	0.26	0.25	0.32	0.35	0.37	0.3	0.32	0.39	0.34	0.24	0.3	0.33	0.44	0.28	0.31	0.51	0.33	0.33	0.29	0.35	0.06
δCe	1.24	1.23	1.23	1.26	1.24	1.25	1.24	1.24	1.25	1.24	1.24	1.25	1.24	1.24	1.25	1.24	1.26	1.27	1.26	1.23	1.27	0.01

$\delta Eu=Eu_N/(Sm_N*Gd_N)^{1/2}$, $\delta Ce=Ce_N/(La_N*Pr_N)^{1/2}$

Intrusion	CXWC pluton													Stdev
Petrology	Monzogranite													n=13
CaO	26.88	27.1	26.85	26.78	27.2	26.76	27.49	26.65	27.45	26.96	26.91	26.96	27.02	0.25

TiO_2	34.95	34.98	34.69	34.41	34.74	34.98	35.34	34.85	35.38	34.91	34.62	34.71	34.73	0.27
Na_2O	0.02	0.02	0.02	bdl	bdl	0.03	0.04	bdl	0.04	bdl	0.04	0.02	0.03	0.01
F	0.3	0.76	0.4	0.59	0.45	0.45	0.54	0.43	0.56	0.16	0.59	0.52	0.59	0.15
MgO	0.03	0.02	0.03	0.02	0.01	bdl	bdl	0.01	0.01	0.01	0.01	0.02	bdl	0.01
Al_2O_3	1.73	1.62	1.74	1.56	1.66	1.55	1.53	1.69	1.58	1.61	1.79	1.62	1.71	0.08
Fe_2O_3	2.27	2.07	2.13	2.18	2.12	1.9	2.02	1.98	2.1	2.08	2.21	2.24	2.07	0.10
MnO	0.16	0.2	0.15	0.11	0.17	0.16	0.18	0.19	0.18	0.15	0.18	0.2	0.18	0.02
P_2O_5	0.05	0.03	0.02	0.02	0.04	0.09	0.05	0.02	0.05	0.03	0.05	0.07	0.04	0.02
SiO_2	30.52	30.85	30.42	30.66	30.76	30.5	31.09	30.63	30.99	30.74	30.64	30.44	30.61	0.20
F=O	0.13	0.32	0.17	0.25	0.19	0.19	0.23	0.18	0.23	0.07	0.25	0.22	0.25	0.06
Total	96.59	97.14	96.08	95.88	96.77	96.05	97.87	96.07	97.89	96.4	96.59	96.37	96.54	0.65
Fe_2O_3/Al_2O_3	1.31	1.28	1.23	1.39	1.28	1.22	1.32	1.17	1.33	1.29	1.24	1.38	1.21	0.07
$Fe_2O_3+Al_2O_3$	4.01	3.68	3.87	3.74	3.78	3.45	3.55	3.66	3.68	3.69	4	3.86	3.79	0.16
Cu	0.58	0.69	0.61	0.64	0.85	0.86	0.73	0.75	0.81	0.81	0.64	0.76	0.76	0.09

This is a preprint, the final version is subject to change, of the American Mineralogist (MSA)
Cite as Authors (Year) Title. American Mineralogist, in press.
DOI: https://doi.org/10.2138/am-2018-6224

Mo	54.8	65.24	61.39	76.77	71.26	79	68.33	67.69	62.82	70.97	75.89	79.13	66.66	7.29
Ga	44.05	41.77	50.35	48.26	47.79	46.53	42.18	56.55	53.91	47.61	47.27	50.29	44.94	4.27
Ge	49.9	46.91	59.8	56.9	55.82	52.91	46.52	64.8	61.36	51.75	53.88	59.75	51.79	5.59
Sr	8.31	9.77	9.24	16.1	12.36	17.12	11.95	18.63	14.09	16.49	6.06	15.57	11.53	3.83
Y	5499	4793	6681	5817	5533	5064	4439	6381	6293	4952	6379	6201	5720	704
Zr	456	445	495	507	474	491	467	489	478	485	489	520	475	20.05
Nb	6491	7695	6441	6846	7709	6462	7683	5304	6744	6996	7281	7160	7263	670
La	939	922	980	922	1006	1038	1002	1105	1070	1120	915	915	888	77.81
Ce	4301	4113	4704	4398	4626	4608	4360	5156	5014	4838	4372	4460	4177	315
Pr	770	720	890	846	842	829	739	986	938	840	812	871	777	75.56
Nd	3735	3433	4648	4481	4266	4162	3512	5232	4874	4091	4057	4706	3930	534
Sm	1076	943	1468	1425	1254	1222	927	1701	1542	1137	1233	1566	1203	241
Eu	75	72	92	119	95	111	80	146	115	99	67	128	87	23.72
Gd	975	839	1351	1294	1113	1078	809	1538	1387	985	1135	1428	1094	228

This is a preprint, the final version is subject to change, of the American Mineralogist (MSA)
Cite as Authors (Year) Title. American Mineralogist, in press.
DOI: https://doi.org/10.2138/am-2018-6224

Tb	162	139	224	212	184	176	131	251	226	160	194	236	186	37.41
Dy	985	844	1336	1246	1092	1024	789	1430	1317	951	1183	1363	1121	205
Ho	195	169	252	230	207	193	157	258	243	182	233	246	215	32.93
Er	537	469	662	578	548	497	434	638	622	489	631	616	566	72.29
Tm	80.92	71.66	94.69	79.41	78.29	70.35	65.51	85.71	87.78	71.98	93.13	83.35	81.14	8.82
Yb	518	471	584	473	488	434	430	500	538	462	584	490	500	48.59
Lu	60.35	55.31	65.25	51.46	55.64	48.71	50.78	53.26	59.96	53.85	66.1	52.26	55.59	5.40
Hf	43.73	40.82	44.94	40.85	41.31	39.03	41.79	39.08	42.37	41.3	47.53	41.57	40.88	2.32
Ta	1154	1388	1262	1357	1528	1186	1395	1036	1275	1289	1400	1426	1476	138
Th	254	245	252	326	269	322	277	358	289	284	228	338	262	39.74
U	187.12	183.82	177.65	168.79	165.45	161.99	180.97	156.53	175.56	180.43	190.25	169.32	169.23	10.13
∑REE	14406	13261	17352	16356	15856	15491	13488	19081	18034	15479	15575	17159	14881	1710
$(La/Sm)_N$	0.56	0.63	0.43	0.42	0.52	0.55	0.7	0.42	0.45	0.64	0.48	0.38	0.48	0.10
$(La/Yb)_N$	1.3	1.41	1.2	1.4	1.48	1.72	1.67	1.58	1.43	1.74	1.12	1.34	1.27	0.20

DOI: https://doi.org/10.2138/am-2018-6224

$(Sm/Yb)_N$	2.31	2.23	2.79	3.35	2.85	3.13	2.39	3.78	3.18	2.74	2.34	3.55	2.67	0.50
δEu	0.22	0.25	0.2	0.27	0.25	0.3	0.28	0.28	0.24	0.29	0.17	0.26	0.23	0.04
δCe	1.24	1.24	1.23	1.22	1.23	1.22	1.24	1.21	1.23	1.22	1.24	1.23	1.23	0.01

$\delta Eu=Eu_N/(Sm_N*Gd_N)^{1/2}$, $\delta Ce=Ce_N/(La_N*Pr_N)^{1/2}$, Abbreviation: bdl= below detection limit

Intrusion	TCG pluton																				Stdev
Petrology	Biotite granitic porphyry																				n=20
CaO	27.75	27.55	26.98	27.61	27.65	27.73	27.11	27.29	27.62	27.92	27.1	27.87	27.55	28.36	27.82	27.79	28.1	28.28	27.94	28.05	0.37
TiO_2	37.06	37.28	35.72	36.95	36.88	36.72	36.81	36.02	36.78	36.73	37.06	35.55	36.62	36.44	37.51	37.61	36.92	37	37.3	37.08	0.54
Na_2O	bdl	bdl	0.03	bdl	0.02	0.03	bdl	0.04	bdl	bdl	0.03	0.03	0.04	bdl	0.02	bdl	bdl	bdl	0.04	0.02	0.01
F	0.39	0.11	0.06	0.5	0.19	0.45	0.37	0.39	0.29	0.32	bdl	0.19	0.5	0.37	0.29	0.45	0.31	0.15	0.56	0.53	0.15
MgO	0.01	bdl	0.01	0.01	0.01	bdl	0.01	bdl	0.01	0.01	bdl	bdl	0.02	bdl	bdl	bdl	0.02	bdl	bdl	0.01	0.00

DOI: https://doi.org/10.2138/am-2018-6224

Al_2O_3	1.38	1.15	1.31	1.25	1.24	1.15	1.25	1.34	1.28	1.16	1.18	1.2	1.18	1.11	1.2	1.18	1.33	1.31	1.35	1.49	0.10
Fe_2O_3	1.83	1.45	2.12	1.73	1.51	1.58	1.68	1.65	1.58	1.54	1.55	1.48	1.66	1.5	1.56	1.5	1.61	1.36	1.62	1.66	0.16
MnO	0.17	0.13	0.15	0.15	0.16	0.13	0.13	0.18	0.14	0.09	0.14	0.12	0.11	0.03	0.13	0.18	0.17	0.14	0.17	0.17	0.04
P_2O_5	0.08	0.08	0.08	0.09	0.07	0.08	0.09	0.08	0.11	0.07	0.08	0.07	0.06	0.03	0.08	0.09	0.06	0.08	0.09	0.07	0.02
SiO_2	31.04	31.05	30.64	31.17	30.96	31.31	30.72	30.65	31.44	30.89	30.63	30.18	29.71	31.72	30.88	31.15	31.19	30.69	31.12	31.26	0.45
F=O	0.16	0.05	0.03	0.21	0.08	0.19	0.16	0.16	0.12	0.14	0.01	0.08	0.21	0.15	0.12	0.19	0.13	0.06	0.24	0.22	0.07
Total	99.37	98.64	96.87	99.1	98.47	98.85	97.85	97.32	99	98.46	97.64	96.47	97.09	99.27	99.22	99.62	99.44	98.81	99.81	99.96	1.02
Fe_2O_3/Al_2O_3	1.33	1.26	1.62	1.38	1.22	1.37	1.34	1.23	1.23	1.33	1.32	1.24	1.41	1.35	1.3	1.27	1.21	1.04	1.21	1.11	0.12
$Fe_2O_3+Al_2O_3$	3.21	2.61	3.42	2.98	2.75	2.74	2.93	2.98	2.87	2.7	2.73	2.68	2.84	2.61	2.75	2.68	2.94	2.67	2.97	3.16	0.22
Cu	0.73	0.73	0.89	0.7	0.58	0.97	0.7	0.78	0.65	0.78	0.7	0.76	0.8	1.15	21.46	33.78	11.02	1.17	1.33	5.27	8.59
Mo	51.32	72.28	47.67	61.41	71.04	68.52	50.88	50.3	68.95	60.18	63.47	96.36	73.02	85.48	69.43	77.19	85.07	62.57	79.32	87.76	13.55
Ga	59.54	53.37	69.92	47.07	44.32	46.61	55.09	44.64	41.24	63.05	67.13	38.69	61.12	65.7	41.82	45.49	64.16	40.21	45.52	51.44	10.12
Ge	60.93	49.79	65	41.17	42.15	43.69	49.7	41.88	41.63	59.67	65.07	41.8	56.59	33.22	37.18	41.83	42.88	42.12	49.03	29.99	10.02
Sr	91.53	77.81	91.91	74.63	67.32	75.9	81.72	75.39	76.12	82.56	91.51	66.45	86.63	77.25	69.29	82.25	70.44	75	70.86	63.34	8.46

DOI: https://doi.org/10.2138/am-2018-6224

Y	3020	1876	1995	1483	1602	1593	1943	1762	1849	2086	2444	1946	1834	1495	1444	1771	2637	2249	2591	1580	432
Zr	694	467	544	432	396	438	457	390	419	501	540	374	607	606	398	437	479	393	1400	653	225
Nb	3776	3405	2838	2551	2853	2847	2246	2193	2535	2995	3411	3903	3827	3338	2580	3361	2899	2537	3037	3020	502
La	1813	2110	2748	2014	1581	1751	2083	1667	1441	2272	2545	1132	2315	1297	1542	1625	1088	1198	1204	1074	502
Ce	6824	6889	8908	6232	5442	5903	6945	5584	4996	7844	8545	4334	7737	4268	5087	5452	4149	4485	4807	3659	1532
Pr	1094	961	1268	827	779	838	994	794	743	1161	1246	695	1100	604	708	781	700	713	816	531	212
Nd	5171	4075	5501	3340	3396	3571	4298	3409	3340	5105	5535	3314	4720	2600	2972	3384	3511	3396	4064	2326	930
Sm	1170	767	1034	586	662	668	824	654	691	1006	1099	774	884	515	537	672	923	791	1012	487	201
Eu	265	171	175	134	148	154	184	152	160	207	242	181	187	130	129	161	227	192	237	125	40.38
Gd	930	574	738	434	492	489	605	491	536	720	821	607	627	404	404	518	785	654	814	396	157
Tb	131	78	97	58	66	64	82	68	74	96	109	83	82	55	54	71	114	92	116	56	22.45
Dy	695	407	493	306	344	341	433	361	400	485	573	437	415	301	288	376	615	501	608	314	117
Ho	122	73	82	56	61	60	76	66	72	84	100	77	72	55	53	68	108	89	106	59	19.48
Er	292	179	182	138	149	148	184	164	176	193	232	182	168	139	132	166	256	214	245	149	43.24

Tm	36.72	23.35	22.1	18.69	19.87	19.79	23.87	21.74	23.33	24.75	29.07	23.77	21.72	19.17	18.41	22.37	32.37	27.75	30.66	20.41	4.94
Yb	209	141	122	118	125	123	143	135	147	142	168	142	130	125	115	137	184	166	177	129	24.83
Lu	23.31	17.19	13.11	14.95	15.47	15.4	17.34	16.57	18.25	16.5	19.48	17.19	15.91	15.69	14.73	17.11	20.2	19.36	19.92	15.94	2.35
Hf	57.71	33.1	51.83	30.39	28.92	31.48	29.99	26.45	27.79	33.88	34.89	27.91	42.11	39.46	26.8	30.39	31.49	27.21	51.18	45.8	9.41
Ta	544	301	310	200	225	225	194	179	204	247	340	350	348	337	205	298	311	237	322	276	84.21
Th	440	477	370	429	430	446	384	324	330	409	535	493	513	351	329	406	298	304	292	358	73.67
U	89	98	55	92	105	107	83	82	101	87	96	139	109	121	93	106	110	96	110	152	20.63
∑REE	18776	16465	21383	14277	13280	14144	16890	13583	12817	19354	21264	11999	18475	10529	12054	13448	12712	12536	14255	9343	3446
$(La/Sm)_N$	1	1.78	1.72	2.22	1.54	1.69	1.63	1.65	1.35	1.46	1.49	0.94	1.69	1.63	1.85	1.56	0.76	0.98	0.77	1.42	0.38
$(La/Yb)_N$	6.22	10.75	16.14	12.25	9.11	10.21	10.43	8.86	7.05	11.52	10.87	5.74	12.75	7.47	9.58	8.49	4.23	5.18	4.89	5.98	3.08
$(Sm/Yb)_N$	6.22	6.05	9.41	5.53	5.9	6.03	6.39	5.38	5.24	7.9	7.28	6.08	7.54	4.59	5.17	5.44	5.56	5.3	6.37	4.2	1.20
δEu	0.78	0.79	0.61	0.81	0.8	0.82	0.8	0.82	0.8	0.74	0.78	0.81	0.77	0.87	0.85	0.84	0.82	0.82	0.8	0.87	0.05
δCe	1.19	1.19	1.17	1.18	1.2	1.19	1.18	1.19	1.18	1.18	1.18	1.2	1.19	1.18	1.19	1.19	1.17	1.19	1.19	1.19	0.01

$\delta Eu=Eu_N/(Sm_N*Gd_N)^{1/2}$, $\delta Ce=Ce_N/(La_N*Pr_N)^{1/2}$, Abbreviation: bdl= below detection limit

This is a preprint, the final version is subject to change, of the American Mineralogist (MSA)
Cite as Authors (Year) Title. American Mineralogist, in press.
DOI: https://doi.org/10.2138/am-2018-6224

Intrusion	PL pluton																			Stdev
Petrology	Quartz monzonitic porphyry																			n=19
CaO	26.31	26.35	27.35	26.41	27.66	26.22	27.39	26.77	26.6	28.1	26.62	27	27.99	26.04	26.42	27.95	26.55	28.01	26.8	0.69
TiO_2	35.32	35.19	36.36	34.81	36.82	34.56	35.86	35.16	35.59	36.58	35.83	36.37	36.65	35.29	35.01	37.31	33.85	37.99	35.03	1.03
Na_2O	0.02	bdl	0.04	0.1	bdl	0.05	bdl	bdl	bdl	bdl	bdl	bdl	bdl	0.02	bdl	0.02	bdl	bdl	bdl	0.03
F	0.15	bdl	0.08	0.13	0.21	0.15	0.08	0.13	bdl	0.13	bdl	0.26	0.35	bdl	0.18	0.08	0.2	0.24	0.17	0.07
MgO	bdl	bdl	bdl	bdl	0.01	bdl	bdl	0.01	0.02	bdl	bdl	bdl	bdl	bdl	bdl	0.01	0.01	0.02	bdl	0.01
Al_2O_3	1.24	1.24	1.03	1.28	1.02	1.27	1.15	1.15	1.02	1.09	1.19	1.14	0.95	1.17	1.36	1.04	1.42	0.93	1.31	0.14
Fe_2O_3	2.04	2.12	1.61	2.05	1.53	2.02	1.73	1.74	1.47	1.7	1.51	1.57	1.63	1.72	2.21	1.69	2.28	1.39	1.96	0.27
MnO	bdl	bdl	0.04	bdl	0.03	bdl	bdl	bdl	bdl	0.03	bdl	0.04	0.05	0.03	bdl	0.03	bdl	0.05	bdl	0.01
P_2O_5	0.03	0.05	0.08	0.08	0.07	0.09	0.1	0.03	0.12	0.1	0.09	0.11	0.1	0.13	0.06	0.13	0.05	0.1	0.05	0.03
SiO_2	29.99	29.59	31.03	30.06	30.72	29.54	30.63	29.96	29.57	30.83	29.79	29.74	30.05	29.02	29.33	30.54	30.04	30.31	29.97	0.53

F=O	0.06	0.02	0.03	0.06	0.09	0.06	0.04	0.06	bdl	0.05	bdl	0.11	0.15	bdl	0.07	0.03	0.08	0.1	0.07	0.03
Total	94.85	94.36	97.44	94.66	97.83	93.66	96.74	94.74	94.25	98.35	94.89	95.97	97.46	93.26	94.3	98.62	94.1	98.82	95.05	1.82
Fe_2O_3/Al_2O_3	1.65	1.71	1.57	1.6	1.5	1.6	1.51	1.51	1.44	1.57	1.27	1.38	1.71	1.47	1.63	1.62	1.6	1.5	1.5	0.11
$Fe_2O_3+Al_2O_3$	3.28	3.35	2.64	3.33	2.55	3.29	2.88	2.88	2.49	2.79	2.7	2.7	2.58	2.89	3.57	2.73	3.7	2.32	3.27	0.39
Cu	0.66	0.69	0.81	0.82	0.74	0.75	0.84	0.62	0.6	0.68	0.64	0.82	0.77	0.81	0.74	0.82	0.75	0.71	0.84	0.08
Mo	48.45	48.64	65.53	64.22	66.9	55.74	69.12	53.98	73.19	68.97	75.29	72.22	70.27	24.49	53.56	66.08	48.9	68.43	49.06	12.68
Ga	57.23	69.14	29.39	66.73	37.71	66.08	35.46	50.11	72.89	26.15	83.78	44.48	25.44	56.11	48.53	28.4	68.73	24.99	67.45	18.85
Ge	57.09	74.64	26.66	71.81	35.87	71.31	32.65	50.2	73.53	23.5	85.72	41.53	22.69	65.5	48.37	25.26	71.82	22	72.62	21.83
Sr	64.36	60.93	65.17	58.68	67.69	55.19	61.78	56.89	86.09	65.64	78.14	64.16	62.83	46.6	56.57	63.65	57.15	60.91	58.62	8.46
Y	3017	4281	1153	4019	1668	3960	1403	2445	3228	924	4091	1751	899	4334	2334	1019	4148	841	4384	1386
Zr	592	583	584	612	595	598	612	606	582	592	666	569	591	474	548	576	583	575	555	36.43
Nb	1157	1241	1028	1756	1215	1481	1193	1163	2234	935	2762	1484	945	2673	1036	1018	1266	961	1249	558
La	1940	2062	1377	2055	1598	2021	1563	1889	2678	1303	2982	1965	1313	1397	1877	1415	2106	1337	1981	459
Ce	6723	7626	3883	7528	4840	7318	4575	6120	8767	3446	10085	5833	3466	5970	6086	3878	7668	3474	7417	1945

Pr	1042	1274	507	1247	668	1215	616	902	1350	434	1589	793	424	1080	891	486	1261	417	1249	371
Nd	4896	6413	2133	6193	2879	6030	2587	4105	6263	1766	7551	3376	1700	5525	3965	1961	6248	1652	6297	1992
Sm	1136	1660	427	1569	585	1513	507	902	1401	337	1747	672	316	1419	842	368	1578	302	1650	546
Eu	192	268	82	253	107	245	92	154	226	65	280	121	61	232	147	70	257	59	269	83.38
Gd	855	1301	318	1223	435	1176	368	681	1010	250	1287	484	231	1127	624	271	1231	224	1297	428
Tb	121	189	44	176	60	170	50	95	139	34	181	66	31	166	87	36	177	30	189	62.80
Dy	652	1012	232	944	323	912	270	512	731	180	953	359	169	940	470	194	959	162	1025	339
Ho	119	178	43	167	61	162	51	94	128	34	168	65	32	174	87	36	169	30	181	59.27
Er	296	426	111	402	160	391	134	237	313	89	401	168	85	437	226	98	412	80	438	140
Tm	40.65	55.69	16.22	52.57	24.11	51.69	19.73	33.38	42.15	13.16	52.47	23.88	12.87	59.1	31.96	14.59	54.03	11.97	57.54	17.65
Yb	250	321	109	307	166	298	136	208	256	92	302	154	93	353	204	103	317	85	336	95.56
Lu	29.09	35.9	14.83	34.31	22	33.71	18.07	25.66	29.11	12.85	33.76	19.3	13.62	39.52	25.11	14.5	35.18	12.22	37.11	9.40
Hf	43.74	43.44	38.51	47.22	41.36	49.85	41.43	45.18	49.87	38.8	56.36	41.13	38.96	36.86	40.29	39.05	44.49	38	42.53	4.98
Ta	169	176	100	249	139	230	132	161	338	88	466	179	90	308	128	101	192	84	182	98.80

Th	500	491	487	535	502	486	521	531	609	481	736	587	501	470	552	514	498	519	498	61.75
U	66.22	61.92	74.14	65.04	76.8	61.86	77.65	68.33	65.91	76.24	70	75	80	71	71	77	64	80	62	6.31
∑REE	18291	22822	9295	22151	11929	21537	10986	15959	23334	8053	27610	14100	7947	18918	15564	8945	22470	7876	22421	6380
$(La/Sm)_N$	1.1	0.8	2.08	0.85	1.76	0.86	1.99	1.35	1.23	2.5	1.1	1.89	2.68	0.64	1.44	2.48	0.86	2.86	0.78	0.72
$(La/Yb)_N$	5.57	4.61	9.1	4.8	6.89	4.87	8.22	6.52	7.51	10.2	7.08	9.17	10.1	2.84	6.61	9.81	4.77	11.28	4.23	2.41
$(Sm/Yb)_N$	5.06	5.75	4.37	5.67	3.91	5.64	4.13	4.82	6.09	4.08	6.42	4.86	3.76	4.47	4.59	3.95	5.54	3.95	5.46	0.82
δEu	0.6	0.56	0.68	0.56	0.65	0.56	0.65	0.6	0.58	0.69	0.57	0.65	0.69	0.56	0.62	0.68	0.56	0.69	0.56	0.05
δCe	1.16	1.15	1.14	1.15	1.15	1.14	1.14	1.15	1.13	1.12	1.14	1.15	1.14	1.19	1.15	1.15	1.15	1.14	1.16	0.01

$\delta Eu=Eu_N/(Sm_N*Gd_N)^{1/2}$, $\delta Ce=Ce_N/(La_N*Pr_N)^{1/2}$, Abbreviation: bdl= below detection limit

Intrusion	TXWC pluton																	Stdev
Petrology	Biotite granite																	n=17
CaO	25.49	26.79	26.56	26.51	26.81	26.45	26.55	26.13	26.74	26.91	26.56	26.42	27.01	26.77	26.61	26.63	25.98	0.37
TiO_2	35.1	35.37	34.81	34.64	35.51	34.69	34.34	33.54	35.65	34.95	35.73	33.37	35.97	35.08	34.97	33.31	33.29	0.88
Na_2O	bdl	bdl	0.03	bdl	bdl	0.02	bdl	0.03	bdl	bdl	bdl	bdl	0.03	0.02	bdl	0.03	0.02	0.01
F	0.09	0.16	0.19	0.27	0.21	0.15	0.2	0.13	0.06	0.31	0.1	0.13	0.15	0.16	0.16	0.18	bdl	0.06
MgO	bdl	bdl	bdl	bdl	bdl	bdl	bdl	bdl	bdl	bdl	bdl	0.01	bdl	bdl	bdl	bdl	bdl	0.00
Al_2O_3	1.13	1.4	1.24	1.31	1.26	1.12	1.42	1.39	1.28	1.24	1.15	1.36	1.17	1.43	1.1	1.31	1.25	0.11
Fe_2O_3	1.94	1.94	2.38	2.24	2.01	1.86	2.31	2.02	2.08	2.31	1.61	2.68	1.72	2.16	2.18	2.33	2.25	0.26
MnO	bdl	bdl	0.16	0.08	bdl	bdl	0.06	bdl	0.11	0.12	bdl	0.13	bdl	bdl	0.09	0.05	0.11	0.03
P_2O_5	0.1	0.01	0.06	0.07	0.07	0.08	0.05	0.05	0.04	0.02	0.12	0.05	0.06	0.06	0.06	0.05	0.05	0.03
SiO_2	28.84	30.17	30.05	29.87	29.93	30.02	29.77	29.99	29.78	30.17	29.41	30.26	30.14	30.49	29.49	30.33	30.12	0.40
F=O	0.04	0.07	0.08	0.11	0.09	0.06	0.08	0.05	0.03	0.13	0.04	0.05	0.06	0.07	0.07	0.07	0.01	0.03

This is a preprint, the final version is subject to change, of the American Mineralogist (MSA)
Cite as Authors (Year) Title. American Mineralogist, in press.
DOI: https://doi.org/10.2138/am-2018-6224

Total	92.47	95.59	95.18	94.67	95.54	94.15	94.41	93.03	95.52	95.69	94.51	94.12	96.03	95.92	94.39	93.92	92.88	1.09
Fe_2O_3/Al_2O_3	1.71	1.39	1.92	1.7	1.59	1.67	1.63	1.46	1.63	1.86	1.4	1.97	1.47	1.52	1.99	1.78	1.79	0.19
$Fe_2O_3+Al_2O_3$	3.07	3.34	3.61	3.55	3.27	2.98	3.73	3.4	3.35	3.56	2.76	4.04	2.89	3.59	3.27	3.64	3.5	0.33
Cu	0.68	0.76	0.6	0.84	0.71	0.81	0.59	0.77	0.59	0.59	0.76	0.71	0.77	0.83	0.74	0.82	0.74	0.09
Mo	23.81	19.29	15.63	16.47	22.12	20.68	20.68	18.61	20.69	21.58	23.7	13.3	26.8	18.1	16.94	16.23	15.43	3.57
Ga	77.28	56.95	58.85	54.11	53.97	56.14	53.26	59.51	62.78	58.45	52.44	58.02	69.84	57.55	57.78	55.33	57.62	6.24
Ge	89.44	67.84	70.76	63	63.95	66.74	62.84	68.84	74	68.43	60.91	68.54	80.85	66.7	68.63	67.57	68.15	6.92
Sr	44.9	41.61	10.38	8.87	24.28	42.08	10.67	44.97	14.72	15.46	41.75	6.91	67.04	24.4	16.83	6.6	6.98	18.28
Y	6127	5099	6779	6211	5132	4853	5860	4829	5340	4669	4588	7363	4784	5794	6393	7048	6851	916
Zr	662	456	445	409	450	456	433	459	439	400	456	434	510	475	467	443	394	59.47
Nb	5743	2341	3697	4612	3373	2869	4465	2264	7031	8872	2983	4984	2974	2763	3338	7435	6092	1963
La	1822	1220	1219	1168	1179	1253	1134	1331	1668	1570	1154	1279	1605	1213	1242	1267	1298	204
Ce	7906	5598	5795	5494	5470	5665	5345	5922	6967	6544	5175	6020	7039	5645	5875	5908	6117	710
Pr	1455	1056	1084	997	1018	1056	988	1101	1160	1096	964	1083	1306	1070	1095	1033	1085	120

This is a preprint, the final version is subject to change, of the American Mineralogist (MSA)
Cite as Authors (Year) Title. American Mineralogist, in press.
DOI: https://doi.org/10.2138/am-2018-6224

Nd	7626	5637	5513	4976	5307	5534	5021	5824	5497	5163	5047	5337	7013	5683	5693	5043	5270	707
Sm	2053	1556	1499	1313	1470	1488	1341	1553	1276	1162	1359	1392	1845	1578	1545	1274	1332	218
Eu	292	243	140	112	184	234	126	241	140	133	213	115	306	199	167	105	114	65.10
Gd	1664	1287	1294	1126	1218	1210	1146	1254	1018	907	1116	1206	1441	1328	1317	1117	1139	169
Tb	249	193	203	178	185	182	178	186	151	133	168	192	207	205	203	175	178	25.15
Dy	1390	1098	1222	1074	1068	1031	1067	1049	897	779	966	1195	1132	1195	1207	1092	1101	137
Ho	253	205	247	221	202	194	214	193	183	158	182	252	199	227	238	233	231	27.28
Er	622	513	680	622	518	491	585	480	526	457	464	739	478	589	640	703	682	92.17
Tm	80.8	69.85	99.55	93.85	70.87	66.29	86.06	65.14	86.97	74.76	64.21	116.2	61.18	80.8	92.03	115.44	107.63	17.78
Yb	469	413	640	615	430	395	550	387	667	572	397	802	348	488	579	823	742	150
Lu	51.02	47.05	76.17	74.25	48.47	44.72	65.5	43.66	97.87	85.57	45.23	101.01	37.67	55.67	67.66	107.5	93.46	22.96
Hf	56.94	36.92	48.35	48.03	37.92	39.32	44.84	37.24	84.12	79.94	36.63	62.86	40.44	41.58	46.51	75.16	57.28	15.63
Ta	887	283	471	565	384	357	508	262	955	1520	355	815	397	342	411	963	719	335
Th	760	511	402	314	467	535	377	482	314	299	498	320	484	514	451	307	315	121

DOI: https://doi.org/10.2138/am-2018-6224

U	91.36	86.33	136.52	152.5	95.92	85.2	123.19	78.83	369.35	335.12	88.66	202.08	67.5	100.8	122.08	258.88	184.79	90.99
∑REE	25933	19135	19714	18063	18370	18844	17846	19629	20335	18836	17314	19830	23017	19558	19960	18996	19490	2035
$(La/Sm)_N$	0.57	0.51	0.52	0.57	0.52	0.54	0.55	0.55	0.84	0.87	0.55	0.59	0.56	0.5	0.52	0.64	0.63	0.11
$(La/Yb)_N$	2.79	2.12	1.37	1.36	1.96	2.27	1.48	2.47	1.8	1.97	2.09	1.14	3.31	1.78	1.54	1.1	1.25	0.61
$(Sm/Yb)_N$	4.86	4.18	2.6	2.37	3.79	4.18	2.71	4.46	2.13	2.26	3.81	1.93	5.9	3.59	2.97	1.72	1.99	1.20
δEu	0.48	0.52	0.31	0.28	0.42	0.53	0.31	0.53	0.37	0.4	0.53	0.27	0.57	0.42	0.36	0.27	0.28	0.11
δCe	1.19	1.21	1.24	1.25	1.22	1.21	1.24	1.2	1.23	1.22	1.2	1.25	1.19	1.22	1.24	1.27	1.26	0.02

$\delta Eu=Eu_N/(Sm_N*Gd_N)^{1/2}$, $\delta Ce=Ce_N/(La_N*Pr_N)^{1/2}$, Abbreviation: bdl= below detection limit

Table.3 The average contents of REE in titanites and whole rocks (a) and calculational REE partition coefficients of titanite/melt (b)

(a)

TCG	PL	TXWC

DOI: https://doi.org/10.2138/am-2018-6224

	Contents in Whole rock(ppm)	Stdev (n=5)	Contents in titanite (ppm)	Stdev (n=20)	Contents in Whole rock(ppm)	Stdev (n=2)	Contents in titanite (ppm)	Stdev (n=19)	Contents in Whole rock(ppm)	Stdev (n=4)	Contents in titanite (ppm)	Stdev (n=17)
La	68.3	3.52	1725	502	25.5	1.91	1835	459	35.0	6.13	1331	204
Ce	113	5.24	5905	1532	52.6	0.85	6037	1945	64.9	10.5	6029	710
Pr	11.1	0.44	868	212	6.29	0.06	918	371	6.88	1.03	1097	120
Nd	37.4	1.41	3851	930	27.2	1.34	4292	1992	26.2	3.57	5599	707
Sm	5.42	0.32	788	201	5.11	0.21	996	546	4.08	0.42	1473	218
Eu	1.47	0.11	178	40.38	1.09	0.02	167	83.4	0.88	0.07	180	65.1
Gd	3.93	0.35	602	157	3.94	0.12	758	428	2.99	0.32	1223	169
Tb	0.56	0.03	82.3	22.4	0.53	0.01	107	62.8	0.40	0.03	186	25.2
Dy	2.63	0.14	435	117	2.84	0.23	579	339	2.41	0.23	1092	137
Ho	0.48	0.03	77.0	19.5	0.52	0.01	104	59.3	0.48	0.03	214	27.3

DOI: https://doi.org/10.2138/am-2018-6224

Er	1.39	0.08	184	43.24	1.44	0.05	258	140	1.44	0.16	576	92.2
Tm	0.18	0.01	24.0	4.94	0.19	0.00	35.1	17.7	0.20	0.04	84.2	17.8
Yb	1.22	0.08	144	24.8	1.32	0.01	215	95.6	1.50	0.15	534	150
Lu	0.18	0.01	17.2	2.35	0.18	0.01	25.6	9.40	0.22	0.02	67.2	23.0

(b)

Calculational partition coefficients	TCG	PL	TXWC
Kd_{La}	25	72	38
Kd_{Ce}	52	115	93
Kd_{Pr}	79	146	159
Kd_{Nd}	103	158	214
Kd_{Sm}	145	195	361
Kd_{Eu}	121	154	204
Kd_{Gd}	153	193	410
Kd_{Tb}	148	205	463
Kd_{Dy}	166	204	454
Kd_{Ho}	160	202	450
Kd_{Er}	132	180	399
Kd_{Tm}	136	185	432
Kd_{Yb}	118	164	356
Kd_{Lu}	95	146	309

The REE partition coefficients of titanite/melt can be estimated through dividing the average contents of each REE in titanites by those of the whole rocks, assuming that REE contents in the melt could be represented by whole-rock REE contents. The results show that MREE partition coefficients of titanite/melt are higher than those of LREE and HREE, which is consistent with the previous findings (e.g., Green and Pearson 1986; Tiepolo et al. 2002; Prowatke and Klemme 2005; Olin and Wolf 2012)

DOI: https://doi.org/10.2138/am-2018-6224

Table.4 The magmatic temperature and oxygen fugacity calculated by zircon compositions

Pluton	CXWC		TCG		PL		TXWC	
Zircon	n=19	stdev	n=22	stdev	n=21	stdev	n=13	stdev
Ti	4.30	2.72	3.76	0.86	4.85	1.62	4.29	1.61

La	0.14	0.19	0.14	0.15	0.06	0.10	0.10	0.09
Ce	36.6	32.69	41.5	8.8	30.4	7.1	79.0	38.0
Pr	0.31	0.32	0.13	0.05	0.09	0.08	0.20	0.18
Nd	3.86	4.38	1.73	0.43	1.48	0.97	3.29	3.05
Sm	6.16	5.72	3.66	0.90	3.33	1.44	6.35	4.81
Eu	1.49	1.75	1.96	0.45	1.48	0.61	2.46	1.76
Gd	28.8	21.66	19.9	4.4	19.1	6.5	33.9	21.0
Tb	9.59	6.50	7.05	1.62	6.62	1.95	11.37	6.22
Dy	113	70	84	19	81	22	139	69
Ho	42.4	23.9	32.5	6.8	31.8	8.0	56.2	25.4
Er	196	103	154	30	154	36	275	114
Tm	43.0	21.5	34.0	6.1	34.6	7.7	62.8	23.9
Yb	416	202	347	56	343	73	633	226
Lu	86.7	41.1	79.1	11.7	74.4	15.5	140.1	46.5
Hf	11823	1146	12708	724	11882	432	12367	713
U	1321	999	1026	185	426	106	1391	559
Th	657	516	476	142	406	198	1514	841
T(℃)	732		720		742		731	
$(Ce/Ce^*)_D$	40.3		74.7		100.0		133.7	
$\log(fO_2)$	-15.1		-13.3		-11.0		-10.4	

(a) The formula of Ti-in-zircon thermometry is cited from Ferry and Watson (2007). a_{TiO2} is selected to be 0.7 due to the absence of igneous rutile but presence of igneous titanite in rocks

(b) The formula of calculating magmatic oxygen fugacity is cited from Trail et al. (2012).